Banner appropriate to article type will appear here in typeset article

Scalings of small-scale shear layers in temporally developing turbulent boundary layers

Yonggi Park[1] † , Tomoaki Watanabe[1] ‡ and Koji Nagata[1]

[1]Department of Mechanical Engineering and Science, Kyoto University, Kyoto 615-8540, Japan

(Received xx; revised xx; accepted xx)

Small-scale shear layers in temporally developing turbulent boundary layers are investigated using direct numerical simulations at momentum-thickness Reynolds numbers from 2000 to 13000. Flow statistics are evaluated in a local coordinate system aligned with each shear layer identified by the shear intensity. Conditional mean fields show that shear layers are embedded in a biaxial strain. Near the wall, these conditional fields further reveal two distinct regions of intense rigid-body rotation beneath the shear layer, leading to momentum transfer through a mechanism consistent with counter-rotating vortex pairs. Two distinct scalings are found for the shear layers. In the logarithmic and outer layers, the mean shear-related velocity jump Δu_3 and its width δ_3 scale with the Kolmogorov velocity $u_{\eta T}$ and length η_T evaluated in the turbulent region. In the buffer layer, δ_3 scales with the viscous length $\delta_\nu = \nu/u_\tau$ (ν is the kinematic viscosity and u_τ the friction velocity), and Δu_3 scales with $\delta_\nu/\tau_{\eta T}$, consistent with the predominance of shear in energy dissipation, where $\tau_{\eta T}$ is the Kolmogorov time scale. Velocity jumps associated with the biaxial strain exhibit Kolmogorov-based scaling in the logarithmic and outer layers. In the buffer layer, their widths scale with δ_ν, but their velocity jumps do not scale with $\delta_\nu/\tau_{\eta T}$ because strain contributes little to dissipation. Comparisons with turbulent jets indicate weak wall influence in the logarithmic and outer layers. These scalings provide a basis for predicting shear-layer properties, which is crucial for developing flow-control strategies that leverage small-scale shear instability.

1. Introduction

Turbulent flows are ubiquitous in nature and engineering applications, ranging from atmospheric and oceanic currents to flows around vehicles and through pipelines (Davidson 2004). In these diverse contexts, the dynamics of turbulence at small scales play a governing role in determining transport phenomena. For instance, in chemical reactors and combustion engines, the efficiency of mixing and chemical reactions is fundamentally dictated by fluid motions at the smallest scales, where molecular diffusion takes place (Baldyga & Pohorecki 1995; Driscoll 2008). Similarly, in environmental sciences, the dispersion of pollutants and heat transfer in the atmospheric boundary layer are strongly influenced by small-scale

† Email address for correspondence: park.yonggi.67s@st.kyoto-u.ac.jp
‡ Email address for correspondence: watanabe.tomoaki.8x@kyoto-u.ac.jp

Abstract must not spill onto p.2

turbulent fluctuations (Blocken *et al.* 2008; Chillà & Schumacher 2012). Therefore, a deep understanding of small-scale features is indispensable for improving predictive models and developing efficient control strategies for these industrial and environmental systems.

Turbulent motions at small scales govern many important dynamical processes, such as kinetic energy dissipation and enstrophy production (Johnson & Wilczek 2024). The activity of small-scale motions is not spatially uniform but exhibits strong intermittency (Tsinober 2009). From a statistical perspective, small-scale intermittency is often characterised by the probability distributions of velocity gradients and the scaling of high-order structure functions. On the other hand, it can also be examined from a structural perspective, in which coherent flow patterns define various turbulent structures. Enstrophy $\omega^2 = \boldsymbol{\omega} \cdot \boldsymbol{\omega}/2$, defined using the vorticity vector $\boldsymbol{\omega} = \boldsymbol{\nabla} \times \boldsymbol{u}$, is often utilised to extract small-scale vortical structures. One typical small-scale structure in turbulence is a vortex tube, identified as a tubular region of large enstrophy. Besides vortex tubes, large enstrophy values are also concentrated in sheet-like regions, called vortex sheets (Ruetsch & Maxey 1991). Vortex tubes exhibit large enstrophy associated with rigid-body rotation, whereas the vorticity in vortex sheets is associated with shearing motion (Nagata *et al.* 2020; Gul *et al.* 2020). For this reason, vortex sheets are also called small-scale shear layers (Watanabe *et al.* 2020*b*). Early attempts to study small-scale vortical structures focused extensively on vortex tubes, as attested by the large number of publications on this topic (Jiménez *et al.* 1993; Kida & Miura 1998; Tanahashi *et al.* 2001; Ganapathisubramani *et al.* 2008; da Silva *et al.* 2011; Jahanbakhshi *et al.* 2015; Watanabe *et al.* 2017*b*,*a*; Ghira *et al.* 2022).

These studies quantified the characteristics of vortex tubes using conditional averages taken over vortex tubes, whereas early studies of small-scale shear layers largely relied on flow visualisations (Vincent & Meneguzzi 1994). More recently, there have been significant advances in identification schemes for small-scale shear layers based on the triple decomposition method (TDM) of the velocity gradient tensor (Kolář 2007). The TDM describes the motion of a fluid element as three constituents, shear, rigid-body rotation and elongation, and decomposes the velocity gradient tensor $\boldsymbol{\nabla u}$ into these components. This method, originally proposed for identifying vortex tubes associated with rigid-body rotation, successfully distinguishes shear from rotation, both of which contribute to vorticity (Nagata *et al.* 2020; Das & Girimaji 2020). The TDM enables the extraction of small-scale shear layers separately from vortex tubes (Eisma *et al.* 2015; Watanabe *et al.* 2020*b*; Fiscaletti *et al.* 2021). Importantly, the shear component of $\boldsymbol{\nabla u}$ can identify both the location and orientation of each shear layer. Conditional averages in a local coordinate system aligned with each individual shear layer have revealed statistical properties of shear layers, such as the mean flow topology (Watanabe *et al.* 2020*b*).

Extensive studies have been conducted on shear layers using the TDM in canonical flows such as isotropic turbulence (Watanabe *et al.* 2020*b*), turbulent free shear flows (Fiscaletti *et al.* 2021; Hayashi *et al.* 2021*a*,*b*) and turbulent boundary layers (TBLs) (Eisma *et al.* 2015). These studies identified a significant change in the layer-parallel velocity across shear layers. The shear layers experience strain that compresses the fluid in the direction perpendicular to the layer and stretches it in the shear-vorticity direction. Analyses of the flow volume occupied by shear layers and the associated shear-induced velocity have shown their dynamical importance in the budgets of turbulent kinetic energy and enstrophy (Pirozzoli *et al.* 2010; Enoki *et al.* 2023). Additionally, interactions between shearing and straining motions play an important role in interscale energy transfer (Watanabe *et al.* 2020*a*; Enoki *et al.* 2023; Arun *et al.* 2025). A key subject of debate has been the scaling law, namely which turbulence scales characterise shear layers, such as their thickness and the velocity jump. Here, a quantity A is regarded as scaling with B when A/B is approximately constant. Analyses of isotropic turbulence and turbulent free shear flows provided conclusive evidence that the mean velocity jump and its width associated with shear scale with the Kolmogorov velocity and length scales (Watanabe *et al.* 2020*b*; Fiscaletti *et al.* 2021; Hayashi *et al.* 2021*a*). However, an experimental study of a TBL reported that the layer thickness scales with the Taylor microscale (Eisma *et al.* 2015).

Shear layers in wall turbulence are expected to exist between uniform momentum zones, and Taylor-microscale scaling has also been reported for the interfaces of uniform momentum zones (Meinhart & Adrian 1995; De Silva *et al.* 2017; Hearst *et al.* 2021). The aforementioned studies of wall-free turbulence measured the layer thickness using the velocity and shear-intensity distributions in the layer-normal direction. Even in the presence of mean shear, the shear in small-scale shear layers is dominated by velocity fluctuations, and the layer orientation does not align with the mean shear (Fiscaletti *et al.* 2021; Hayashi *et al.* 2021*a*). Nonetheless, in wall turbulence the thickness is typically measured from the streamwise-velocity jump along the wall-normal direction. This may strongly affect thickness estimates because of projection effects from tilted structures. In addition, most studies of shear layers in wall turbulence focus on shear between uniform momentum zones (de Silva *et al.* 2016; Chen *et al.* 2021; Fan *et al.* 2019). However, shearing motion is not produced only by such large-scale structures with different velocities but is also generated by small-scale vortices (Watanabe & Nagata 2022). Evaluating shear layers only at the edges of uniform momentum zones, while excluding their interiors, can bias the resulting statistics. The scalings of shear layers in turbulence without walls have been systematically assessed using DNS of isotropic turbulence and turbulent free shear flows over a range of Reynolds numbers. Comparable attempts have not yet been reported for wall turbulence, leading to a limited understanding of small-scale shear layers in wall turbulence.

Small-scale shear layers are unstable, and their roll-up and subsequent breakdown lead to the formation of vortex tubes (Vincent & Meneguzzi 1994; Passot *et al.* 1995; Watanabe *et al.* 2020*b*). This instability is analogous, in a small-scale sense, to the instability of free shear layers, which has been extensively studied in canonical shear flows (Ho & Huerre 1984). This vortex formation from small-scale shear layers is strongly influenced by velocity fluctuations around shear layers. In particular, fluctuations with a scale of about seven times the layer thickness efficiently promote vortex formation (Watanabe & Nagata 2023). This feature has been shown to be useful for modulating turbulence through external disturbances. By introducing velocity perturbations at the unstable wavelength of the shear layers, vortex formation and shear-layer breakdown are promoted, enhancing small-scale turbulent activity. Specifically, DNS of isotropic turbulence and of a turbulent front evolving into a non-turbulent flow have shown that promoting small-scale shear instability enhances turbulent kinetic energy dissipation, vortex stretching, small-scale scalar mixing and turbulent entrainment (Watanabe & Nagata 2023; Watanabe 2024; Watanabe & Nagata 2025). These effects can be significant: excitation of small-scale shear instability increased the entrainment rate by more than 10% in a turbulent front (Watanabe 2024), and increased the scalar dissipation rate by more than 50% in passive-scalar mixing (Watanabe & Nagata 2025).

Small-scale shear layers in isotropic turbulence and turbulent free shear flows have a characteristic velocity that scales with the Kolmogorov velocity. As the ratio between the Kolmogorov velocity and a characteristic large-scale velocity, e.g. the root-mean-square (r.m.s.) velocity fluctuation, decreases with Reynolds number, even weaker perturbations can promote the instability of small-scale shear layers at higher Reynolds number. These considerations suggest that leveraging small-scale instability is a promising strategy for efficient turbulence control using small-scale disturbances. This approach is also expected to be useful for wall-bounded turbulence. However, investigations of the scaling of small-scale shear layers are required, as it is essential for estimating the unstable wavelength of small-scale shear layers and the perturbation intensity required to promote small-scale shear instability. The scaling of the layer thickness determines the unstable wavelength, whereas the scaling of the velocity jump determines the disturbance intensity required to promote the instability. Therefore, identifying the length and velocity scales of small-scale shear layers in wall turbulence is essential for extending this control concept to wall-bounded flows.

Most previous studies of small-scale shear layers using the TDM have focused on flows without wall influence, such as homogeneous isotropic turbulence, turbulent jets and mixing layers (Watanabe *et al.* 2020*b*; Fiscaletti *et al.* 2021; Hayashi *et al.* 2021*a*,*b*). Although Eisma *et al.* (2015) investigated shear layers in a TBL, the scaling of shear-layer properties in wall turbulence remains unclear. In particular, previous studies of wall-free turbulence reported Kolmogorov scaling of shear-layer thickness and velocity jump, whereas Eisma *et al.* (2015) reported Taylor-microscale scaling in a TBL. This difference raises the question of whether small-scale shear layers identified from velocity-gradient information retain universal small-scale features in wall turbulence, or whether they are modified by wall effects and near-wall turbulent motions. This question is also related to recent discussions on the universality of small-scale statistics in wall turbulence when normalised by local dissipation-based scales (Tang & Antonia 2022).

The present study analyses DNS databases of temporally developing TBLs with Reynolds numbers based on momentum thickness ranging from 2000 to 13000 to elucidate the statistical characteristics of small-scale shear layers. We apply shear-layer identification based on the TDM and evaluate flow statistics in a three-dimensional local shear coordinate system aligned with the shear-layer orientation (Watanabe *et al.* 2020*b*; Hayashi *et al.* 2021*a*). This approach measures shear-layer thickness without bias from wall-normal projection effects and enables evaluation of statistics for all shear layers, not only those nearly parallel to the wall, such as shear regions at the edges of uniform momentum zones. We investigate how the small-scale shear layers depend on wall-normal position and Reynolds number. By examining their properties from the buffer layer to the outer layer, we aim to assess whether the universal characteristics previously observed in homogeneous isotropic turbulence and free shear flows are maintained in wall turbulence. The present results show that two different scalings of small-scale shear layers emerge depending on wall-normal position: Kolmogorov scaling in the logarithmic and outer layers, and a near-wall scaling based on the viscous length and the small-scale shear time scale in the buffer layer.

The paper is organised as follows. Sections 2 and 3 describe the DNS databases of TBLs and the numerical details of the shear-layer analyses, respectively. Section 4 presents statistics of small-scale shear layers, including the mean flow topology and the dependence on Reynolds number and wall-normal position, which are compared with those in homogeneous isotropic turbulence and turbulent planar jets. Finally, the main findings are summarised in § 5.

2. DNS of temporally developing turbulent boundary layer

2.1. *Temporally developing turbulent boundary layer*

The DNS databases used in the present study are those reported and validated in our previous studies (Watanabe *et al.* 2019; Zhang *et al.* 2023). Therefore, this section summarises only the details required for the present shear-layer analysis. Further numerical details, including code validation and velocity statistics, are available in those references.

The DNS considered a temporally developing boundary layer of an incompressible fluid over a wall that moves horizontally at a constant speed U_W. The streamwise, wall-normal and spanwise directions are denoted by x, y and z, respectively, and the corresponding velocity components are u, v and w. The kinematic viscosity and fluid density are denoted by ν and ρ, respectively. Periodic boundary conditions are imposed in the streamwise (x) and spanwise

Table 1: DNS databases of temporally developing TBLs. The Reynolds number based on momentum thickness, Re_θ, is the value at the end of each simulation. The computational domain size is (L_x, L_y, L_z), and the number of grid points is (N_x, N_y, N_z). The friction Reynolds number, Re_τ, and the Reynolds number based on the 99% boundary-layer thickness, Re_δ, are also listed.

Case	B02	B04	B06	B08	B10	B13
Re_θ	2000	4000	6000	8000	10000	13000
L_x/D	56	120	170	220	276	360
L_y/D	76	162	230	298	360	480
L_z/D	28	60	85	110	138	180
N_x	1024	1536	2048	2916	3456	4608
N_y	648	864	1152	1728	2048	2700
N_z	512	1024	1536	1458	2592	3456
Re_τ	706	1312	1845	2538	3058	3980
Re_δ	16517	33774	49567	71175	85528	113182

(z) directions. A no-slip condition is applied at the wall ($y = 0$), and a slip condition is imposed at the top of the computational domain. The flow is initialised with a mean velocity field induced by a trip wire of diameter D (Kozul *et al.* 2016; Zhang *et al.* 2018) and random fluctuations. Here, spatial averages over an x–z plane are denoted by $\langle f \rangle$ and depend on time and wall-normal location. For a variable f, the fluctuating component is defined as $f' = f - \langle f \rangle$, and its r.m.s. value is $f_{rms} = \sqrt{\langle f'^2 \rangle}$. A TBL develops from the initial velocity field over time.

2.2. *Numerical methods and parameters*

The governing equations were the three-dimensional incompressible Navier–Stokes equations, which were solved with an in-house DNS code based on a fractional-step method with staggered grids. Details of the code and its validation, including comparisons with existing data for canonical turbulent flows, are provided in our previous studies (Watanabe *et al.* 2015, 2016; Hayashi *et al.* 2021*a*; Zhang *et al.* 2023). Spatial derivatives were computed using fully conservative central-difference schemes with fourth-order accuracy in the x and z directions and second-order accuracy in the y direction. Time was advanced using a third-order Runge–Kutta method. The biconjugate gradient stabilised method was used to solve the Poisson equation for pressure.

A computational domain was a cuboid of size (L_x, L_y, L_z), resolved by (N_x, N_y, N_z) grid points. As the TBL develops, the Reynolds number based on the boundary-layer thickness increases. Six simulations with different final Reynolds numbers were conducted, as summarised in table 1. All DNS cases were conducted at a Reynolds number based on the trip-wire diameter, $Re_D = U_W D/\nu = 2000$. The momentum thickness is defined as $\theta = \int_0^\infty \langle u \rangle (U_W - \langle u \rangle) U_W^{-2} dy$, and the Reynolds number based on θ is $Re_\theta = U_W \theta/\nu$. In each case, time integration was continued until Re_θ attained the specified target value shown in table 1. Because the boundary-layer thickness increases with Re_θ, a larger domain is required for cases with larger Re_θ. The domain size was determined from the 99% boundary-layer thickness based on the mean velocity profile, δ, such that the domain boundaries do not affect the flow evolution. Uniform grid spacing was applied in the x and z directions. Non-uniform grid spacing was applied to the y direction such that the grid spacing decreases towards the wall. The grid sizes were shown to be small enough to capture small-scale velocity fluctuations in both the near-wall region and the outer layer (Zhang *et al.* 2018, 2023).

The instantaneous flow field was stored when Re_θ reached the target value, and these field data are analysed in the present study. Table 1 also lists the friction Reynolds number $Re_\tau = u_\tau \delta/\nu$ and the Reynolds number based on the boundary-layer thickness, $Re_\delta = U_W \delta/\nu$, at the end of each simulation. Here, $u_\tau = \sqrt{\tau_W/\rho}$ is the friction velocity, and $\tau_W = \rho\nu(\partial\langle u\rangle/\partial y)_W$ is the wall-shear stress, where the subscript W denotes a quantity evaluated at the wall.

2.3. *Averages within turbulent regions of the TBLs*

The present study focuses on small-scale shear layers that appear inside the TBLs. Because of external intermittency, turbulent and non-turbulent fluid intermittently appear at a fixed wall-normal location (da Silva *et al.* 2014). Shear layers do not exist in the non-turbulent region (Hayashi *et al.* 2021*b*). To compare shear layers with turbulence length and velocity scales, we introduce averages evaluated solely over the turbulent region to exclude contributions from non-turbulent fluid.

We identify the turbulent region using the vorticity magnitude ω as $\omega > \omega_{th}$ (da Silva *et al.* 2014). Based on the threshold dependence of the identified turbulent region, we adopt $\omega_{th} = 0.01\omega_r$, where $\omega_r = \langle\omega\rangle$ at $y/\delta = 0.5$ (Zhang *et al.* 2023). At each wall-normal location, horizontal-plane averages are computed using only points with $\omega > 0.01\omega_r$. This average over the turbulent region is denoted by $\langle f\rangle_T$, and the corresponding r.m.s. fluctuation is $f_{rmsT} = \sqrt{\langle f^2\rangle_T - \langle f\rangle_T^2}$. Because the volume fraction of the identified turbulent region varies only weakly with ω_{th} around $\omega_{th} = 0.01\omega_r$, these turbulent-region averages are insensitive to modest changes in the threshold.

With these averages, the Kolmogorov length and velocity scales are defined as $\eta_T = \nu^{3/4}\langle\varepsilon\rangle_T^{-1/4}$ and $u_{\eta T} = (\nu\langle\varepsilon\rangle_T)^{1/4}$, respectively, where $\varepsilon = 2\nu S_{ij}S_{ij}$ is the kinetic energy dissipation rate and $S_{ij} = (\partial u_i/\partial x_j + \partial u_j/\partial x_i)/2$ is the rate-of-strain tensor. The Kolmogorov time scale is defined as $\tau_{\eta T} = \eta_T/u_{\eta T}$. The Taylor microscale is evaluated as $\lambda_T = \sqrt{15\nu u_{0T}^2/\langle\varepsilon\rangle_T}$, where $u_{0T} = \sqrt{(u_{rmsT}^2 + v_{rmsT}^2 + w_{rmsT}^2)/3}$ is the characteristic large-scale velocity.

The scales η_T, $u_{\eta T}$ and $\tau_{\eta T}$ are local scales evaluated as functions of wall-normal position, rather than single reference scales for the entire TBL. The use of turbulent-region averages is important because the TBL exhibits external intermittency, with turbulent and non-turbulent fluids coexisting at a fixed wall-normal location. Our previous analysis of the turbulent/non-turbulent interface in the temporally developing TBLs showed that this intermittency is apparent for $y/\delta \gtrsim 0.6$ (Watanabe *et al.* 2018). In this region, averages over the entire horizontal plane are affected by the non-turbulent fluid and do not represent the turbulence properties. For $y/\delta \lesssim 0.6$, the flow is almost always turbulent, and averages over the entire horizontal plane and over the turbulent region are nearly identical. Since the present study also examines the intermittent outer region, the local Kolmogorov scales based on turbulent-region averages are used throughout the analysis.

2.4. *Mean velocity profile*

The wall-normal distribution of the mean velocity is shown to provide a reference for the wall-normal locations used in the shear-layer analysis. Figure 1 shows profiles of the mean streamwise velocity, compared with those from other experiments and DNS. The wall-normal location y is normalised by the viscous length scale $\delta_\nu = \nu/u_\tau$ as $y^+ = y/\delta_\nu$, while the

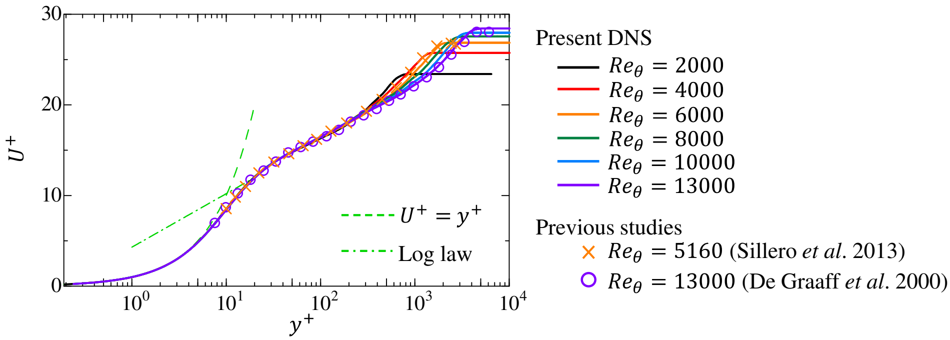

Figure 1: Wall-normal profiles of mean streamwise velocity, $U^+ = (U_W - \langle u \rangle)/u_\tau$, compared with previous DNS (Sillero *et al.* 2013) and experiments (De Graaff & Eaton 2000) at comparable Re_θ. For reference, the viscous-sublayer relation $U^+ = y^+$ and the logarithmic law $U^+ = (1/k)\ln y^+ + A$, with $k = 0.39$ and $A = 4.3$, are shown.

mean velocity is normalised with the friction velocity as $U^+ = (U_W - \langle u \rangle)/u_\tau$. Throughout this paper, superscript + indicates quantities in wall units. Here, the present temporal TBLs are compared with spatially developing TBLs. The present DNS exhibits a typical mean velocity profile of TBLs, including $U^+ = y^+$ in the viscous sublayer and the logarithmic law $U^+ = (1/k)\ln y^+ + A$, with $k = 0.39$ and $A = 4.3$ (Marusic *et al.* 2013). More extensive validation, including r.m.s. velocity fluctuations, Reynolds stress, energy spectra and velocity-gradient statistics, has been presented in our previous studies (Watanabe *et al.* 2019; Zhang *et al.* 2023).

3. Detection and analyses of small-scale shear layers

The small-scale shear layers are analysed with the TDM, by which local motions of fluid elements are represented by three components: shear (S), rigid-body rotation (R) and elongation (E) (Kolář 2007). This decomposition splits the velocity gradient tensor $\boldsymbol{\nabla u}$ into three components as $\boldsymbol{\nabla u} = \boldsymbol{\nabla u}_S + \boldsymbol{\nabla u}_R + \boldsymbol{\nabla u}_E$. The numerical procedure of the TDM adopted in this study is available in previous studies (Nagata *et al.* 2020; Hayashi *et al.* 2021*a*; Fiscaletti *et al.* 2021; Watanabe *et al.* 2025). The intensities of shear, rigid-body rotation and elongation are evaluated as $I_S = \sqrt{2(\boldsymbol{\nabla u}_S)_{ij}(\boldsymbol{\nabla u}_S)_{ij}}$, $I_R = \sqrt{2(\boldsymbol{\nabla u}_R)_{ij}(\boldsymbol{\nabla u}_R)_{ij}}$ and $I_E = \sqrt{2(\boldsymbol{\nabla u}_E)_{ij}(\boldsymbol{\nabla u}_E)_{ij}}$, respectively.

Small-scale shear layers can be detected as flow regions with large I_S (Eisma *et al.* 2015; Watanabe *et al.* 2020*b*). The present study analyses the flow field around local maxima of I_S. The methodology is the same as in our previous studies (Watanabe *et al.* 2020*b*; Hayashi *et al.* 2021*a*; Watanabe & Nagata 2023; Watanabe *et al.* 2025), where further details are provided.

For each detected local maximum, a local shear coordinate system $(\zeta_1, \zeta_2, \zeta_3)$ is introduced to align all shear layers in turbulence in a common orientation. The coordinate origin $(\zeta_1, \zeta_2, \zeta_3) = (0, 0, 0)$ is located at the local maximum. The velocity vector in the shear coordinates is denoted by (u_1, u_2, u_3). To characterise the local flow pattern around a shear layer, these velocity components are taken as the relative velocity with respect to $(\zeta_1, \zeta_2, \zeta_3) = (0, 0, 0)$. The unit vectors of the shear coordinates are denoted by $\boldsymbol{e}_1$, $\boldsymbol{e}_2$ and $\boldsymbol{e}_3$. In this coordinate system, the shear is predominantly expressed by $\partial u_3/\partial \zeta_2$, which contributes to vorticity in the ζ_1 direction. Therefore, the ζ_1 direction is defined by the unit shear-vorticity vector, $\boldsymbol{e}_1 = \boldsymbol{\omega}_S/|\boldsymbol{\omega}_S|$, where $(\omega_S)_i = \epsilon_{ijk}(\boldsymbol{\nabla u}_S)_{jk}$ is the shear-vorticity vector and ϵ_{ijk}

is the Levi–Civita symbol. The shear-coordinate system is not unique, because physically equivalent coordinate systems exist. To remove this ambiguity, we consider only coordinate systems with $(\boldsymbol{e}_2)_y > 0$. This coordinate is identified with the numerical algorithm described in previous studies (Watanabe *et al.* 2020*b*; Hayashi *et al.* 2021*a*).

Following identification of the shear coordinate system at each local maximum of I_S, flow variables $f(x, y, z)$ on the DNS grid are interpolated onto the shear coordinates $(\zeta_1, \zeta_2, \zeta_3)$, i.e. $f(\zeta_1, \zeta_2, \zeta_3)$, using a third-order polynomial interpolation scheme. This interpolation is applied for all local maxima of I_S. Subsequently, ensemble averages of $f(\zeta_1, \zeta_2, \zeta_3)$ are computed over all identified local maxima at each wall-normal location and denoted by $\overline{f}(y; \zeta_1, \zeta_2, \zeta_3)$, to indicate explicitly the dependence on wall distance y. Because no shear layers exist outside the TBL, the analysis is restricted to $y/\delta \leqslant 1.1$. In addition, the lowest wall-normal location considered is $y^+ = 15$ to exclude the viscous sublayer, where shear layers arising from velocity fluctuations are scarce owing to the predominance of mean shear. Within this y range, more than 21 discrete points are defined for the shear-layer analysis. At each discrete point $y = y_S$, shear layers are identified within a wall-normal band of ± 10 grid points and sampled to compute conditional statistics in the shear coordinates, which are taken to represent the shear-layer characteristics at $y = y_S$.

4. Results and discussion

4.1. *Three motions extracted by the triple decomposition method*

Figure 2 visualises I_S, I_R and I_E on an x–y plane of the TBL with $Re_\theta = 10000$. In figure 2(*a*), the shear intensity is generally large in the vicinity of the wall, and large I_S often appears as a thin line. In contrast, regions of large I_R often have a circular shape in figure 2(*b*). Comparison of figures 2(*b*) and 2(*c*), together with the enlarged view in figure 2(*d*), shows that I_E tends to be large around these circular regions of large I_R. Large I_S and I_R correspond to two-dimensional cuts of shear layers and vortex tubes, respectively (Nagata *et al.* 2020; Watanabe *et al.* 2020*b*). Regions of large I_E, where energy dissipation due to irrotational strain occurs, tend to surround vortex tubes (Ruetsch & Maxey 1991). The distributions of I_S, I_R and I_E in the TBL are consistent with those observed in homogeneous isotropic turbulence (Watanabe *et al.* 2020*b*) and turbulent planar jets (Hayashi *et al.* 2021*a*).

Figure 3(*a*) shows the wall-normal profiles of the mean intensities of the three motions, $\langle I_S \rangle_T$, $\langle I_R \rangle_T$ and $\langle I_E \rangle_T$, normalised by U_W/δ in the TBLs with $Re_\theta = 4000$ and 10000. Here, the averages are evaluated within the turbulent region because the non-turbulent region has negligible shear and rigid-body rotation. In the viscous sublayer ($y^+ \lesssim 5$), $\langle I_S \rangle_T$ is much larger than $\langle I_R \rangle_T$ and $\langle I_E \rangle_T$. The large values of I_S reflect the predominance of mean shear near the wall. A recent velocity-gradient partitioning analysis of channel flows and TBLs also observed the predominance of shear in the near-wall region (Arun & Colonius 2024). The three intensities decrease with increasing y^+, consistent with the reduction in velocity fluctuations. Throughout the TBL, shear is stronger than the other motions. The mean intensities are larger for the higher Re_θ case because the time scale of small-scale turbulent motions, related to velocity gradients, becomes shorter at a higher Reynolds number.

The peaks of $\langle I_R \rangle_T$ and $\langle I_E \rangle_T$ appear near the wall. In the buffer layer, the velocity-gradient tensor is dominated by shear, and rigid-body rotation and elongation are weak compared with those in turbulent flows without direct wall influence, such as turbulent planar jets (Hayashi *et al.* 2021*a*). As y^+ increases towards the lower part of the logarithmic layer, rigid-body rotation and elongation become relatively more important among the small-scale motions. Farther from the wall, however, the overall magnitude of velocity gradients decreases with increasing y^+, leading to decreases in $\langle I_R \rangle_T$ and $\langle I_E \rangle_T$. The balance between these two

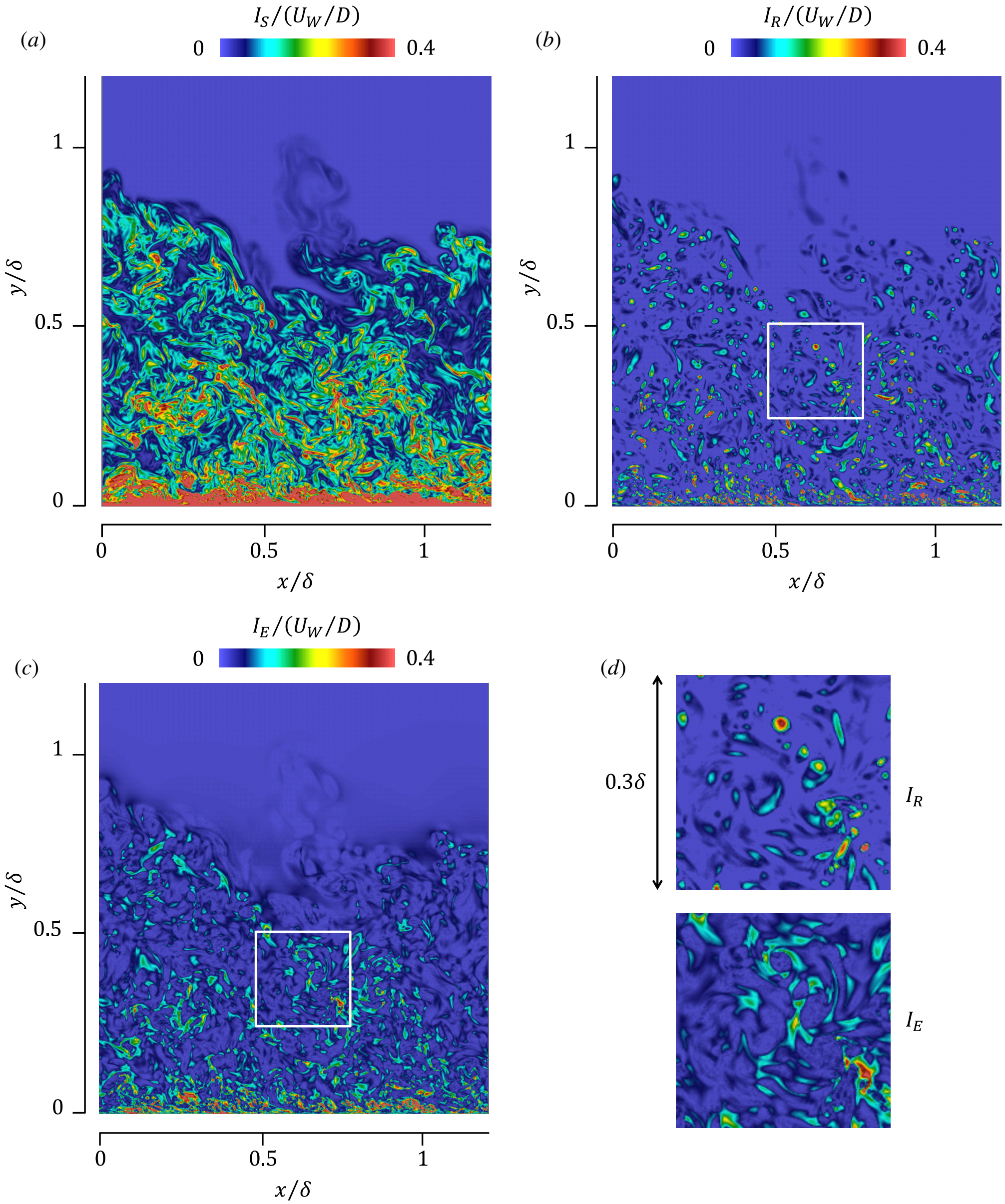

Figure 2: Two-dimensional distributions of the intensities of the three motions extracted by the TDM at $Re_\theta = 10000$: (*a*) shear, I_S, (*b*) rigid-body rotation, I_R and (*c*) elongation, I_E. (*d*) Enlarged view of I_R and I_E in the regions marked by white boxes in (*b*) and (*c*).

effects produces the peaks of $\langle I_R \rangle_T$ and $\langle I_E \rangle_T$ around $y^+ \approx 30$, which are not directly related to the inner peak of r.m.s. velocity fluctuations.

The relative importance of the three motions at a given height is examined in figure 3(*b*) using intensities normalised by the Kolmogorov time scale, $\tau_{\eta T}$. In the viscous sublayer, $\langle I_S \rangle_T / \tau_{\eta T}^{-1} \sim 1.3$ is much larger than the other components. In the buffer layer, shear becomes relatively weaker and the other two motions become more important, as indicated by the

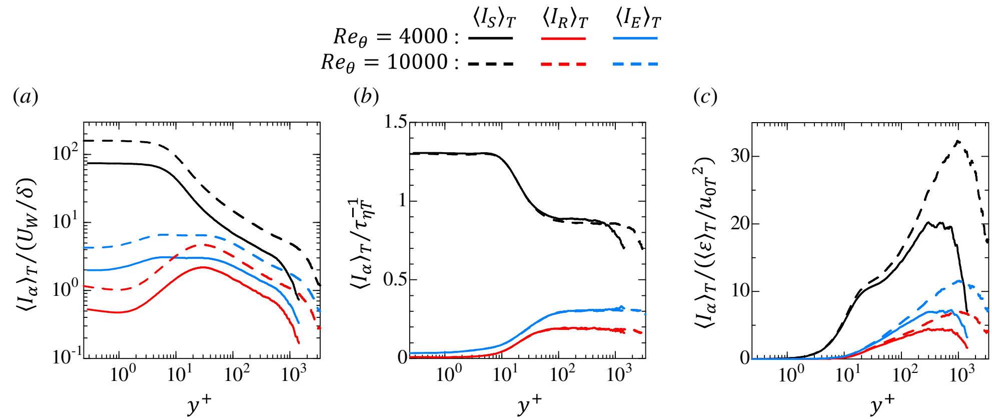

Figure 3: Wall-normal profiles of mean intensities of the three motions, $\langle I_S\rangle_T$, $\langle I_R\rangle_T$ and $\langle I_E\rangle_T$, normalised by (a) U_W/δ, (b) $\tau_{\eta T}^{-1}$, and (c) $\langle\varepsilon\rangle_T/u_{0T}^2$ for $Re_\theta = 4000$ and 10000.

decrease in $\langle I_S\rangle_T/\tau_{\eta T}^{-1}$ and the increase in $\langle I_R\rangle_T/\tau_{\eta T}^{-1}$ and $\langle I_E\rangle_T/\tau_{\eta T}^{-1}$. The mean intensities are then nearly constant in the logarithmic layer and decrease towards the edge of the TBL. The results for the two Re_θ cases collapse well, indicating that the mean intensities scale with the inverse of the Kolmogorov time scale. The difference between $Re_\theta = 4000$ and 10000 appears at large y^+, because the y^+ location of the outer edge of the TBLs depends on Re_θ.

Figure 3(c) adopts the normalisation based on $\langle\varepsilon\rangle_T/u_{0T}^2$. The energy dissipation rate generally scales as $\langle\varepsilon\rangle_T \sim u_{0T}^3/L$, where L is a characteristic length scale of large-scale motions (Davidson 2004). Thus, $\langle\varepsilon\rangle_T/u_{0T}^2 \sim u_{0T}/L$ can be interpreted as the inverse of the y-dependent large-scale time scale. This normalisation leads to significant y-and Re_θ-dependences in the logarithmic and outer layers, indicating that the mean intensities of the three motions are not characterised by the large-scale time scale.

The vorticity vector $\boldsymbol{\omega} = \nabla\times\boldsymbol{u}$ is decomposed into shear and rigid-body-rotation components as $\boldsymbol{\omega} = \boldsymbol{\omega}_S + \boldsymbol{\omega}_R$, where $(\omega_S)_i = \epsilon_{ijk}(\nabla\boldsymbol{u}_S)_{jk}$ and $(\omega_R)_i = \epsilon_{ijk}(\nabla\boldsymbol{u}_R)_{jk}$. The TDM is then used to decompose the velocity field into shear and non-shear components, $\boldsymbol{u} = \boldsymbol{u}_S + \boldsymbol{u}_{NS}$, by reconstructing the shear velocity $\boldsymbol{u}_S = (u_S, v_S, w_S)$ from the shear vorticity $\boldsymbol{\omega}_S = (\omega_{Sx}, \omega_{Sy}, \omega_{Sz})$ through the Biot–Savart relation. This approach follows Enoki *et al.* (2023), but is implemented differently to impose the boundary conditions of the temporal TBL considered here.

Specifically, the Poisson equation

$$\nabla^2 v_S = \frac{\partial\omega_{Sz}}{\partial x} - \frac{\partial\omega_{Sx}}{\partial z}, \tag{4.1}$$

is solved for v_S, and then u_S and w_S are obtained from

$$\left(\frac{\partial^2}{\partial x^2} + \frac{\partial^2}{\partial z^2}\right) u_S = -\frac{\partial^2 v_S}{\partial x\partial y} + \frac{\partial\omega_{Sy}}{\partial z}, \tag{4.2}$$

$$\left(\frac{\partial^2}{\partial x^2} + \frac{\partial^2}{\partial z^2}\right) w_S = -\frac{\partial^2 v_S}{\partial y\partial z} - \frac{\partial\omega_{Sy}}{\partial x}. \tag{4.3}$$

The non-shear component $\boldsymbol{u}_{NS}$ is obtained by subtracting $\boldsymbol{u}_S$ from $\boldsymbol{u}$. A fast Fourier transform in the x and z directions and a tridiagonal matrix algorithm in the y direction are employed to solve (4.1)–(4.3), with $v_S = 0$ imposed at the wall and the upper boundary. The total velocity

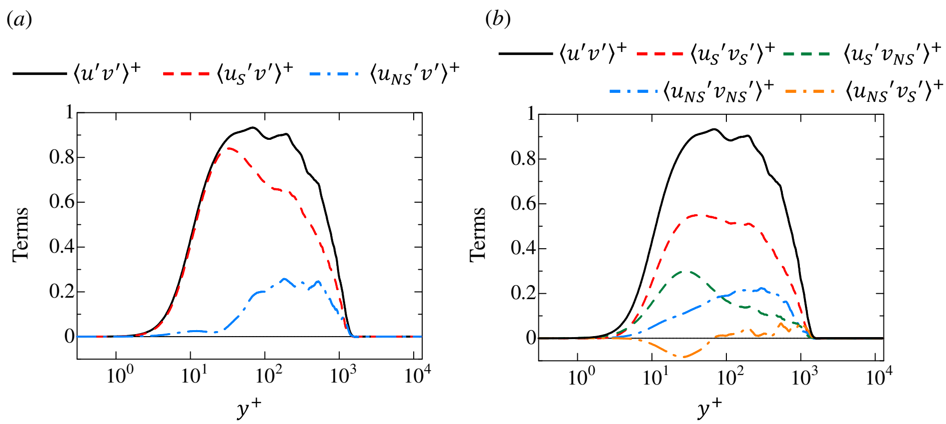

Figure 4: Contributions of shear and non-shear velocities to the Reynolds stress $\langle u'v'\rangle$: (*a*) $\langle u'v'\rangle = \langle u'_S v'\rangle + \langle u'_{NS} v'\rangle$ and (*b*) $\langle u'v'\rangle = \langle u'_S v'_S\rangle + \langle u'_S v'_{NS}\rangle + \langle u'_{NS} v'_S\rangle + \langle u'_{NS} v'_{NS}\rangle$. Wall-normal distributions for $Re_\theta = 4000$ are shown.

vector is thus decomposed as

$$\boldsymbol{u} = \boldsymbol{u}_S + \boldsymbol{u}_{NS} = \langle \boldsymbol{u}_S\rangle + \boldsymbol{u}'_S + \boldsymbol{u}'_{NS}. \tag{4.4}$$

Here, $\langle \boldsymbol{u}_S\rangle = \langle \boldsymbol{u}\rangle$ and $\langle \boldsymbol{u}_{NS}\rangle = \boldsymbol{0}$, because the mean velocity profile is associated solely with the mean shear.

The non-shear velocity $\boldsymbol{u}_{NS}$ is related to the vorticity associated with rigid-body rotation. However, it is not referred to here as the rotational velocity, because the symmetric part of the non-shear velocity-gradient tensor is the elongational component of the TDM. We therefore use the term "non-shear velocity" for this velocity component.

This decomposition is applied to the Reynolds stress $\langle u'v'\rangle$, which represents the vertical transfer of streamwise momentum, as $\langle u'v'\rangle = \langle u'_S v'\rangle + \langle u'_{NS} v'\rangle$. The first and second terms represent the contributions of the shear and non-shear components of streamwise momentum, respectively. Figure 4(*a*) shows the wall-normal profiles of these terms. Here, the present study considers a TBL developing over a wall moving in the x direction. In this configuration, $\langle u'v'\rangle$ is positive, whereas it is negative for a TBL developing over a stationary wall in a freestream. In the viscous sublayer and buffer layer, $y^+ \lesssim 25$, $\langle u'v'\rangle \approx \langle u'_S v'\rangle$, indicating that the vertical momentum transfer is dominated by the shear component of the streamwise momentum. Even in the logarithmic and outer layers, $y^+ \gtrsim 25$, $\langle u'_S v'\rangle$ remains larger than $\langle u'_{NS} v'\rangle$.

Further decomposition of the wall-normal velocity fluctuation yields $\langle u'v'\rangle = \langle u'_S v'_S\rangle + \langle u'_S v'_{NS}\rangle + \langle u'_{NS} v'_S\rangle + \langle u'_{NS} v'_{NS}\rangle$. These terms represent the vertical transfer of streamwise shear/non-shear momentum by wall-normal shear/non-shear velocities. Figure 4(*b*) shows the wall-normal profiles of these decomposed terms. A similar decomposition of the Reynolds stress was examined by Enoki *et al.* (2023) for a turbulent planar jet in the context of turbulent-kinetic-energy production. They showed that $\langle u'_S v'_S\rangle$ makes the dominant contribution to the Reynolds stress. Consistently, the present results also show that $\langle u'_S v'_S\rangle$ is the predominant contribution over most of the TBL. A related analysis of the Reynolds stress in TBLs was reported by Pirozzoli *et al.* (2010), who reconstructed the velocity fields associated with shear layers and vortex tubes from truncated vorticity vectors set to zero outside the structures of interest. They also showed that the velocity field reconstructed from shear layers makes the dominant contribution to the Reynolds stress. These studies suggest that the flow induced by shear layers is more energetic than that induced by vortex tubes, leading

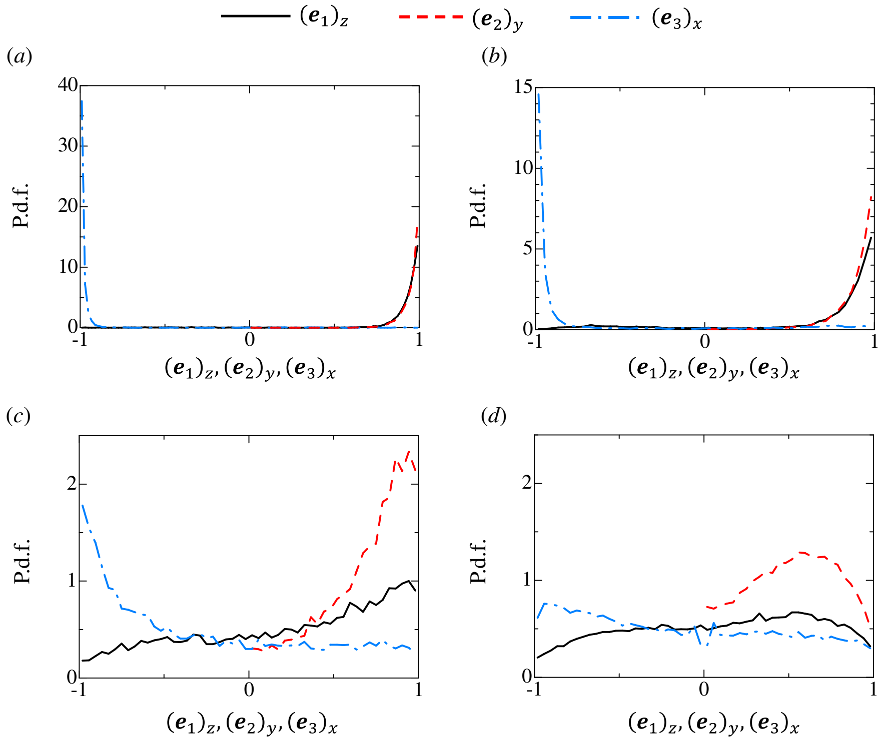

Figure 5: Probability density functions of the z, y and x components of $\boldsymbol{e}_1$, $\boldsymbol{e}_2$ and $\boldsymbol{e}_3$, denoted by $(\boldsymbol{e}_1)_z$, $(\boldsymbol{e}_2)_y$ and $(\boldsymbol{e}_3)x$, at (*a*) $y^+ = 15$ ($y/\delta = 0.0048$), (*b*) $y^+ = 31$ ($y/\delta = 0.01$), (*c*) $y^+ = 153$ ($y/\delta = 0.05$) and (*d*) $y^+ = 1529$ ($y/\delta = 0.5$) for $Re_\theta = 10000$.

to a larger contribution to the turbulent kinetic energy and the Reynolds stress. However, as the wall is approached, $\langle u'_S v'_{NS} \rangle$ becomes relatively more important and exhibits a peak near the lower edge of the logarithmic layer. This term represents the vertical transfer of shear-related streamwise momentum caused by the non-shear wall-normal velocity. This momentum transfer is discussed below in connection with the mean flow pattern around shear layers in the near-wall region.

4.2. *Fundamental statistical properties of small-scale shear layers*

The orientations of shear layers are examined using probability density functions (p.d.f.s) of individual components of the unit vectors of the shear coordinates, $\boldsymbol{e}_1$, $\boldsymbol{e}_2$ and $\boldsymbol{e}_3$, which represent the ζ_1, ζ_2 and ζ_3 directions, respectively. The p.d.f.s are shown for the z, y and x components of $\boldsymbol{e}_1$, $\boldsymbol{e}_2$ and $\boldsymbol{e}_3$, respectively, because these components effectively characterise shear-layer orientation near the wall. In particular, $\boldsymbol{e}_1$, $\boldsymbol{e}_2$ and $\boldsymbol{e}_3$ tend to align preferentially with the z, y and $-x$ directions, respectively, and to be perpendicular to the other directions. Figure 5 presents the p.d.f.s evaluated at four wall-normal locations, $y^+ = 15$, 31, 153 and 1529 ($y/\delta = 0.0048$, 0.01, 0.05 and 0.5). Here, $y^+ = 15$ is within the buffer layer, $y^+ = 31$ is close to the boundary between the buffer and logarithmic layers, and $y^+ = 153$ and 1529 lie in the logarithmic and outer layers, respectively.

The p.d.f.s at $y^+ = 15$ and 31 exhibit distinct peaks at -1 or 1, indicating that shear layers predominantly align with specific directions. The shear-vorticity direction $\boldsymbol{e}_1$ tends to have $(\boldsymbol{e}_1)_z \approx 1$, implying that vorticity due to shear aligns with the spanwise direction. This orientation is consistent with the mean shear, since $\partial \langle u \rangle / \partial y$ contributes to spanwise vorticity.

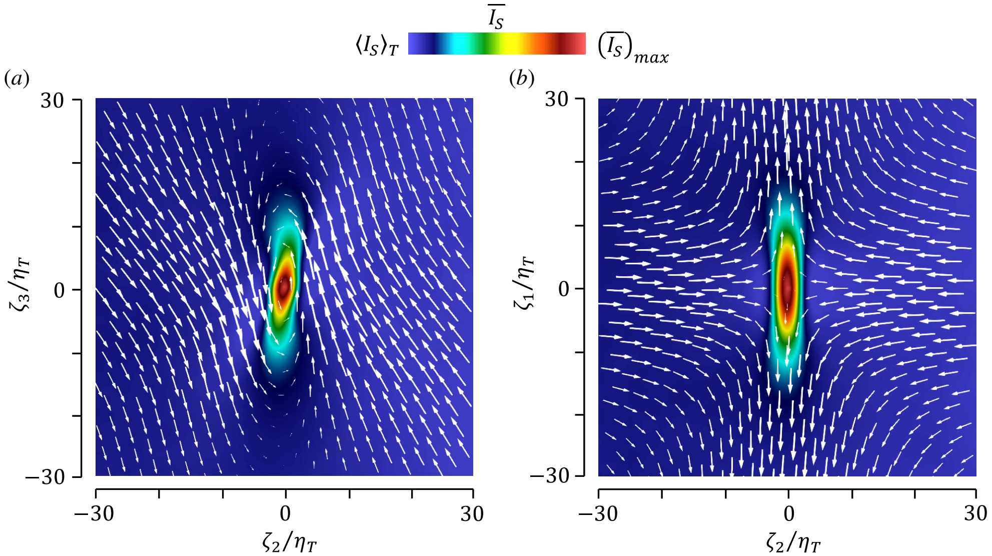

Figure 6: Conditionally averaged flow patterns around small-scale shear layers in the TBL at $Re_\theta = 10000$. Colour contours and arrows represent the mean shear intensity $\overline{I_S}$ and mean velocity vectors $(\overline{u_1}, \overline{u_2}, \overline{u_3})$. The length of a vector indicates the vector magnitude. Results are shown on the (*a*) ζ_2–ζ_3 plane and (*b*) ζ_1–ζ_2 plane for shear layers detected at $y^+ = 1529$ ($y/\delta = 0.5$). The colour range is set using the mean shear intensity $\langle I_S \rangle_T$ and the maximum value of $\overline{I_S}$, $(\overline{I_S})_{\max}$.

Peaks are also observed at $(\boldsymbol{e}_2)_y \approx 1$ and $(\boldsymbol{e}_3)_x \approx -1$. The direction $\boldsymbol{e}_3$ is defined to match the direction of the shear flow, and the peak at $(\boldsymbol{e}_3)_x \approx -1$ indicates that streamwise velocity fluctuations generate locally intense shear. The unit vector $\boldsymbol{e}_2$ represents the direction normal to the shear layers, and the peak at $(\boldsymbol{e}_2)_y \approx 1$ implies that shear layers tend to be parallel to the wall. These results indicate that shear layers near the wall are strongly influenced by the wall. Even at higher locations, $y^+ = 153$ and 1529, the p.d.f.s show similar trends, although the peaks are much weaker than at $y^+ = 15$ and 31. The edges of uniform momentum zones in two-dimensional (x–y) planes are often identified using the wall-normal gradient of the streamwise velocity, $\partial u/\partial y$. Shear layers dominated by $\partial u/\partial y$ would have $(\boldsymbol{e}_2)_y \approx 1$. However, the present results for the logarithmic and outer layers suggest that shear layers are oriented in a range of directions, and that a predominance of $\partial u/\partial y$ in the local shear does not occur.

Conditionally averaged flow patterns around small-scale shear layers are examined using ensemble averages with the method described in § 3. Figure 6 presents two-dimensional profiles of the mean velocity vector $(\overline{u_1}, \overline{u_2}, \overline{u_3})$ and colour contours of the mean shear intensity $\overline{I_S}$ obtained in the TBL at $y^+ = 1529$ with $Re_\theta = 10000$. In isotropic turbulence and turbulent planar jets, shear layers have been shown to comprise two distinct motions, shear and biaxial strain, which can be assessed on the ζ_2–ζ_3 and ζ_1–ζ_2 planes, respectively (Watanabe *et al.* 2020*b*; Hayashi *et al.* 2021*a*). The mean flow patterns on these planes intersecting the shear-layer centre at $(\zeta_1, \zeta_2, \zeta_3) = (0, 0, 0)$ are visualised in figures 6(*a*) and (*b*). The region of large $\overline{I_S}$ has a flattened shape, extended in the ζ_1 and ζ_3 directions. From the centre, $\overline{I_S}$ decreases rapidly in the ζ_2 direction, while the decreases in the ζ_1 and ζ_3 directions are more gradual. The shear-layer size estimated from $\overline{I_S}$ is approximately $30\eta_T \times 5\eta_T \times 30\eta_T$. The shear within this structure is associated with the opposing flows

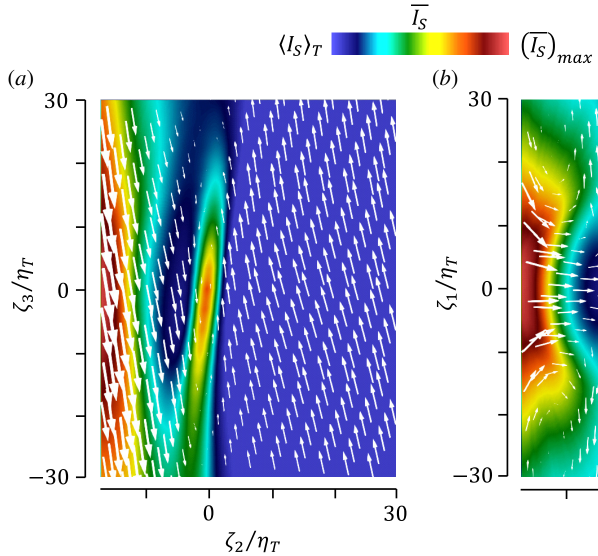

Figure 7: The same as figure 6, but for shear layers detected at $y^+ = 31$ ($y/\delta = 0.01$).

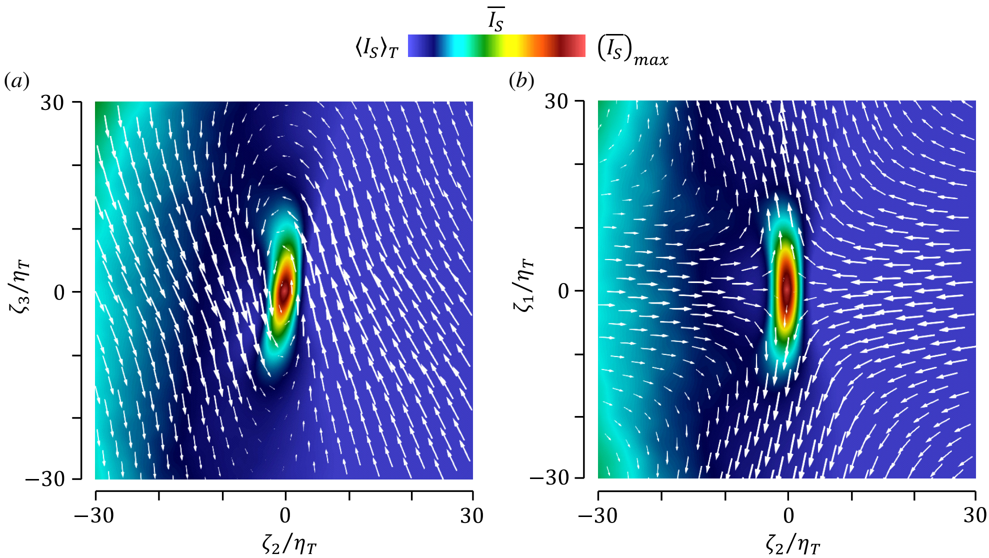

Figure 8: The same as figure 6, but for shear layers detected at $y^+ = 153$ ($y/\delta = 0.05$).

in the $\pm\zeta_3$ directions observed on the ζ_2–ζ_3 plane in figure 6(*a*). The mean velocity field in figure 6(*b*) exhibits a biaxial strain, with stretching in the ζ_1 direction and compression in the ζ_2 direction. This mean pattern of shear and strain is consistent with that observed in isotropic turbulence and turbulent planar jets (Watanabe *et al.* 2020*b*; Hayashi *et al.* 2021*a*).

Figures 7 and 8 show the mean flow patterns of shear layers near the wall, obtained at $y^+ = 31$ and 153 in the DNS with $Re_\theta = 10000$. The range of ζ_2 shown in figure 7 is restricted because no statistical samples are available for $\zeta_2/\eta_T \lesssim -16$ because of the wall. The mean shear-intensity distributions confirm the presence of similar shear layers even near the wall. However, the shear becomes more intense as ζ_2 decreases. Near the wall, the shear

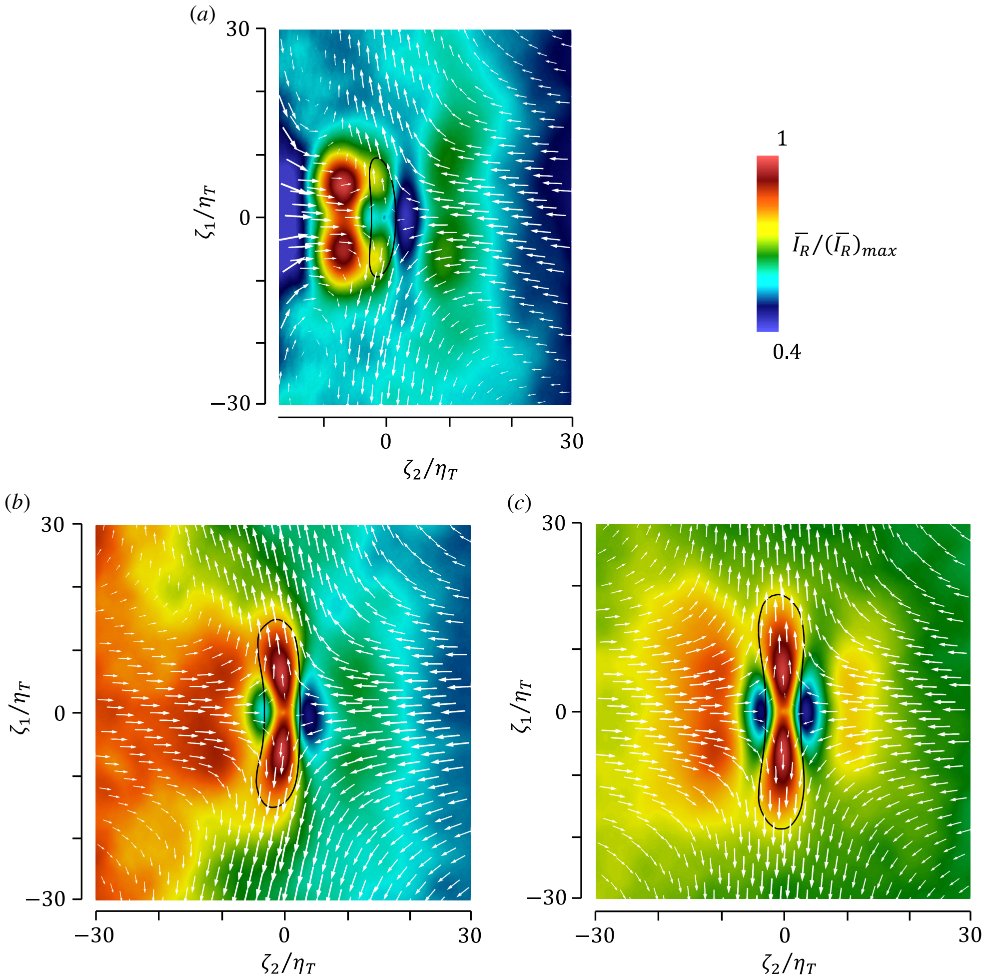

Figure 9: Conditionally averaged intensity of rigid-body rotation near the shear layers on the ζ_1–ζ_2 plane for $Re_\theta = 4000$: (*a*) $y^+ = 31$ ($y/\delta = 0.01$), (*b*) $y^+ = 153$ ($y/\delta = 0.05$) and (*c*) $y^+ = 1529$ ($y/\delta = 0.5$). The black line indicates the shear layer location with the isoline of the mean shear intensity equal to the half of its maximum value at the centre.

coordinates $(\zeta_1, \zeta_2, \zeta_3)$ tend to align with the $(z, y, -x)$ directions. Therefore, the large $\overline{I_S}$ for $\zeta_2 < 0$ outside the shear layer is attributed to stronger shear near the wall, as discussed in figure 3. Nonetheless, the shear layers still experience a biaxial strain.

The decomposition of the Reynolds stress in figure 4 shows that the transfer of shear-related streamwise momentum by the wall-normal non-shear velocity makes an important contribution to momentum transfer in the near-wall region. This coupling is further examined through the conditionally averaged flow pattern around shear layers. Figure 9(*a*) shows the mean intensity of rigid-body rotation on the ζ_1–ζ_2 plane near the shear layers identified at $y^+ = 31$, which is the same wall-normal location as in figure 7. The black line indicates the shear-layer location, represented by an isoline of the mean shear intensity.

In this conditionally averaged field, two regions of intense rigid-body rotation are observed on the wall side of the shear layer at $\zeta_2/\eta_T \approx -8$ and $\zeta_1/\eta_T \approx \pm 5$. The mean velocity vectors around these regions indicate counter-rotating motions, which induce flow towards

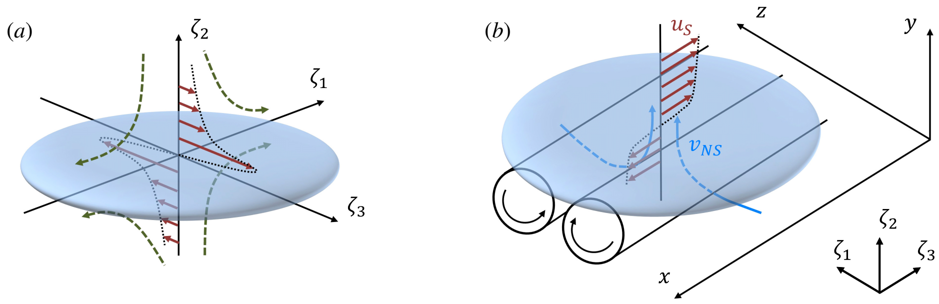

Figure 10: (*a*) A schematic of the mean flow pattern around a shear layer. (*b*) A schematic of the coupling between a shear layer and counter-rotating motions observed in the conditional mean field, leading to wall-normal transfer of streamwise momentum near the wall.

the shear layer with $u_2 > 0$. These regions also exhibit shear flow with $u_3 < 0$, as shown in figure 7(*a*). In the near-wall region, the shear-coordinate directions ζ_1, ζ_2 and ζ_3 preferentially align with the z, y and $-x$ directions, respectively. Therefore, for $\zeta_2 < 0$, the relations $u_2 \sim v > 0$ and $u_3 \sim -u < 0$ imply $uv > 0$. Thus, the rigid-body rotation beneath the shear layer contributes to the Reynolds stress by driving the wall-normal transfer of shear-related streamwise momentum. Moreover, the wall-normal motion $u_2 > 0$ induced by rigid-body rotation is associated with v_{NS}, whereas the streamwise motion due to shear, corresponding to $u_3 < 0$, is associated with u_S. This contribution is therefore related to $\langle u'_S v'_{NS} \rangle$, which is shown to be important near the wall in figure 4(*b*).

The presence of rigid-body rotation beneath the shear layer is consistent with previous observations of coherent structures near the wall. Pairs of counter-rotating streamwise vortices have been observed in conditionally averaged flow patterns near walls (Bakewell Jr. & Lumley 1967; Blackwelder & Eckelmann 1979). The mean flow pattern in figure 9(*a*) is also similar to the classical sketch of counter-rotating vortices interacting with mean shear (Pope 2000; Holmes *et al.* 2012). An important difference, however, is that figure 9(*a*) suggests an interaction between counter-rotating motions and a local shear layer that is strongly influenced by velocity fluctuations, rather than by the mean shear alone, because the shear intensity in the layer is much larger than the mean shear.

Figures 9(*b*, *c*) present the conditionally averaged intensity of rigid-body rotation near the shear layers at $y^+ = 153$ and 1529, for which the conditionally averaged shear-intensity profiles are shown in figures 8 and 6, respectively. Intense rotation is again observed for $\zeta_2 < 0$. The mean velocity vectors for $\zeta_2 < 0$ indicate flow towards the shear layer at all wall-normal locations shown in figure 9. However, because the shear layers are oriented in various directions at large y^+, this local configuration does not lead to a large contribution to $\langle u'_S v'_{NS} \rangle$.

Intense rigid-body rotation is also observed inside the shear layer in figures 9(*b*, *c*), although the mean velocity vectors on the ζ_1–ζ_2 plane do not show a clear rotating pattern there because the rotation axis is not perpendicular to the visualised plane. These rotating motions are relevant to vorticity generated from shear layers: rigid-body rotation with vorticity in the ζ_1 direction grows within the shear layer as shear instability proceeds (Watanabe *et al.* 2020*b*; Watanabe & Nagata 2023). The two regions of intense rigid-body rotation, one for $\zeta_2 < 0$ and the other within the shear layer, are also consistent with anti-parallel vortex tubes observed in various turbulent flows (Goto *et al.* 2017).

Figure 10(*a*) illustrates the mean flow pattern around a shear layer. The mean velocity in the ζ_3 direction, $\overline{u_3}$, rapidly varies across the shear layer in the ζ_2 direction. The mean

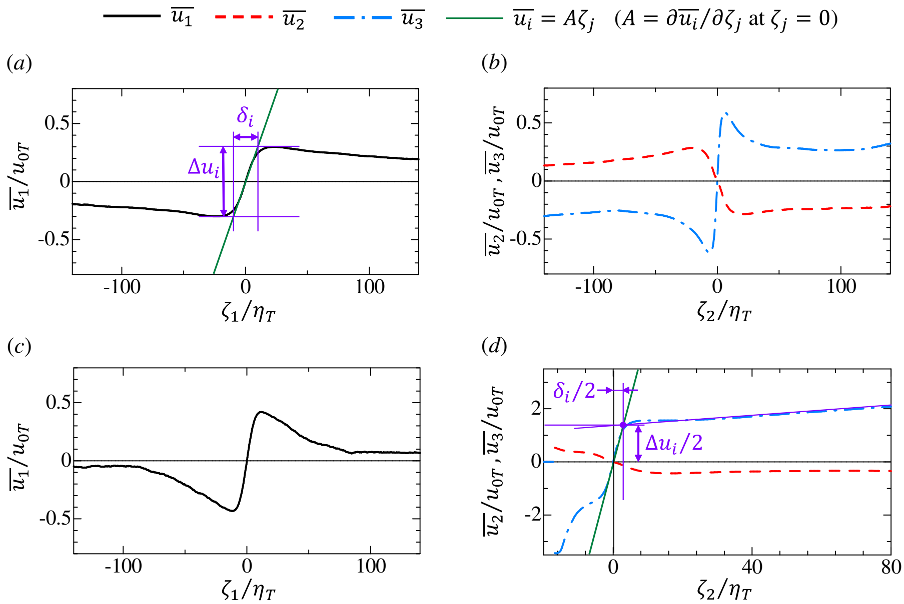

Figure 11: Mean velocity profiles near shear layers at (a, b) $y^+ = 1529$ $(y/\delta = 0.5)$ and (c, d) $y^+ = 31$ $(y/\delta = 0.01)$ for $Re_\theta = 10000$: (a, c) $\overline{u_1}$ along the ζ_1 axis; (b, d) $\overline{u_2}$ and $\overline{u_3}$ along the ζ_2 axis. The evaluation of the mean velocity jump, Δu_i, and its width, δ_i, is illustrated.

velocities in the ζ_1 and ζ_2 directions, denoted by $\overline{u_1}$ and $\overline{u_2}$, respectively, form a biaxial strain around the shear layer, with the mean flow in the ζ_1 direction diverging from the shear-layer centre and that in the ζ_2 direction converging towards it. The p.d.f.s of the shear-coordinate directions in figure 5 indicate the orientation of the shear layer with respect to the (x, y, z) directions. In the near-wall region, the ζ_3 direction preferentially aligns with the direction opposite to the mean flow, namely the $-x$ direction, because the mean shear affects the local shear in the layer. In addition, the ζ_2 direction preferentially aligns with the wall-normal direction, namely the y direction, indicating that the layer is approximately parallel to the wall. These tendencies lead to the preferential alignment of the ζ_1 direction with the spanwise direction, namely the z direction.

Figure 10(b) illustrates the coupling between a shear layer and counter-rotating motions beneath it, as observed in the mean flow pattern near the wall. The shear layer is approximately parallel to the wall. The wall-normal velocity induced by the counter-rotating motions transfers the streamwise momentum associated with the shear layer, leading to a contribution to the Reynolds stress from the shear and non-shear velocity components, denoted by $\langle u'_S v'_{NS} \rangle$ in the Reynolds-stress decomposition based on the triple decomposition. These counter-rotating motions are consistent with previous observations of vortical structures near the wall, connecting the shear layers identified by the TDM to well-known vortical structures in wall turbulence (Bakewell Jr. & Lumley 1967; Blackwelder & Eckelmann 1979; Robinson 1991; Adrian *et al.* 2000).

The mean velocity components associated with the shear and strain exhibit distinct jumps across the shear layer. The shear is observed in $\overline{u_3}$ along the ζ_2 axis, while the strain is reflected in $\overline{u_1}$ along the ζ_1 axis and $\overline{u_2}$ along the ζ_2 axis. Accordingly, the velocity jump and its width are examined using the mean velocity profiles $\overline{u_1}(\zeta_1)$, $\overline{u_2}(\zeta_2)$ and $\overline{u_3}(\zeta_2)$ across the shear-layer centre. Figure 11 shows these mean profiles for shear layers at $y^+ = 1529$ and

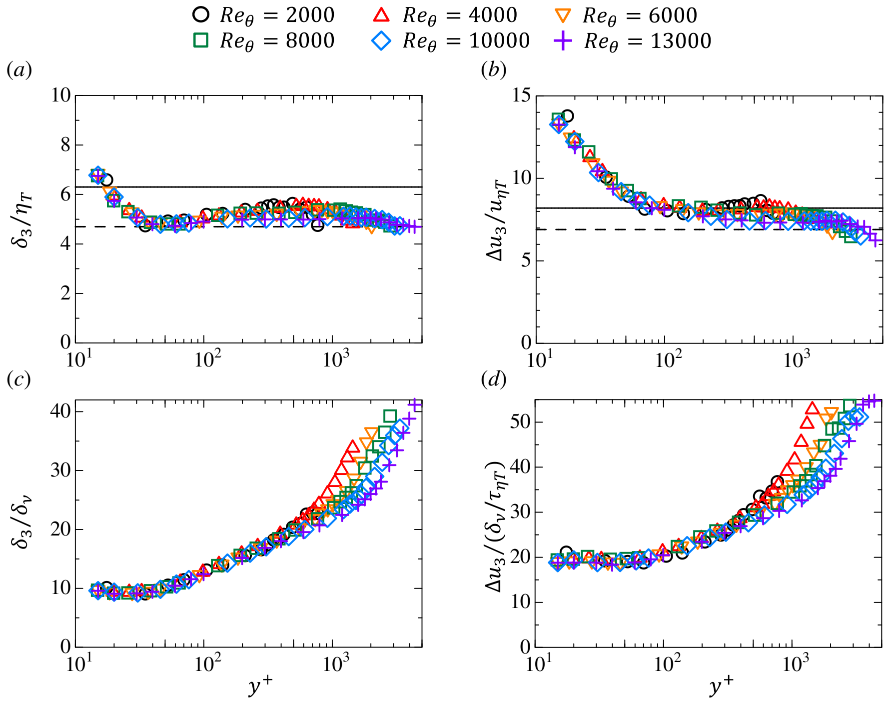

Figure 12: Wall-normal variations of (a, c) the width δ_3 and (b, d) the jump Δu_3 in the mean velocity associated with shear. The Kolmogorov length and velocity scales are used for normalisation in (a) and (b). In (c), δ_3 is normalised by the viscous length scale δ_ν, and the corresponding velocity scale $\delta_\nu/\tau_{\eta T}$ is used to normalise Δu_3 in (d). In (a) and (b), horizontal lines indicate $\delta_3/\eta_T = 4.7$ and 6.3 and $\Delta u_3/u_{\eta T} = 6.9$ and 8.2, corresponding to the minimum and maximum values in transverse profiles of turbulent planar jets (Hayashi *et al.* 2021*a*).

$y^+ = 31$. Large velocity gradients with $\partial\overline{u_1}/\partial\zeta_1 > 0$, $\partial\overline{u_2}/\partial\zeta_2 < 0$ and $\partial\overline{u_3}/\partial\zeta_2 > 0$ further confirm that the shear layer experiences extension in the ζ_1 direction and compression in the ζ_2 direction. The velocity jumps in $\overline{u_i}$ are denoted by Δu_i, and the corresponding widths by δ_i. At $y^+ = 1529$ in figure 11(a) and (b), the mean velocities exhibit positive and negative peaks near the shear layer, and the velocity jump is evaluated as the difference between these peaks. The width of the velocity jump is defined as $\delta_i = \Delta u_i/|\partial\overline{u_i}/\partial\zeta_\alpha|$, where $\alpha = 1$ for $i = 1$ and $\alpha = 2$ for $i = 2$ and 3; the summation convention is not applied. The gradient $|\partial\overline{u_i}/\partial\zeta_\alpha|$ is evaluated at the shear-layer centre. Near the wall, shear layers tend to be approximately horizontal, and the ζ_2 direction preferentially aligns with the y direction. For $\zeta_2 < 0$, the mean-velocity peak may be truncated by the wall. In such cases, the velocity jump and width are estimated as twice those obtained for $\zeta_2 > 0$. In addition, the ζ_3 direction preferentially aligns with the $-x$ direction, so $\overline{u_3}(\zeta_2)$ near the wall is influenced by the wall-normal variation of the mean streamwise velocity. Specifically, for $\zeta_2 > 0$, $\overline{u_3}$ can increase gradually with ζ_2 even outside the shear layer, which obscures the peak used to quantify the velocity jump. In such cases, the velocity jump and width are evaluated using the method of Eisma *et al.* (2015), as illustrated in figure 11(d). The slow increase in $\overline{u_3}$ for $\zeta_2 > 0$ is approximated by a linear fit. The intersection of this fit with $C\zeta_2$, where $C = \partial\overline{u_3}/\partial\zeta_2$ is evaluated at $\zeta_2 = 0$, is denoted by $(\overline{u_3})_P = \overline{u_3}(\zeta_2 = \zeta_P)$. The velocity jump and width are then evaluated as $\Delta u_3 = 2(\overline{u_3})_P$ and $\delta_3 = 2\zeta_P$.

4.3. *Mean velocity jump associated with shear*

The mean velocity jump and width associated with shear, Δu_3 and δ_3, are examined as functions of wall-normal position and Reynolds number. In homogeneous isotropic turbulence and turbulent planar jets over a range of Reynolds numbers, these quantities, when normalised by the corresponding Kolmogorov length and velocity scales, are nearly constant, indicating that δ_3 and Δu_3 scale with the Kolmogorov length and velocity scales, respectively. Figures 12(*a*) and (*b*) show wall-normal profiles of δ_3 and Δu_3 normalised by the Kolmogorov scales, η_T and $u_{\eta T}$. DNS of turbulent planar jets showed that $\delta_3/\eta \approx 4.7$–$6.3$ and $\Delta u_3/u_\eta \approx 6.9$–$8.2$ across the transverse direction for jet Reynolds numbers between 4000 and 100000 (Hayashi *et al.* 2021*a*). These bounds are indicated by horizontal lines in figures 12(*a*) and (*b*). Both $\Delta u_3/u_{\eta T}$ and δ_3/η_T collapse well onto single curves despite differences in Re_θ. Moreover, for $y^+ \gtrsim 50$ across all Reynolds numbers, $\delta_3/\eta_T \approx 5$ and $\Delta u_3/u_{\eta T} \approx 8$ depend only weakly on y^+. These values are consistent with those for turbulent planar jets. In the jets, δ_3/η_T and $\Delta u_3/u_{\eta T}$ decrease slightly towards the jet edge, and a similar trend is observed towards the edge of the TBL. Although $\Delta u_3/u_{\eta T}$ and δ_3/η_T also collapse near the wall, their values vary markedly as y^+ decreases, indicating that the mean shear-related velocity jump is not characterised by the Kolmogorov scales in this region. The consistency between the TBL and jets for $y^+ \gtrsim 50$ suggests that wall effects on the velocity profiles around shear layers are negligible in the logarithmic and outer layers.

Figure 12(*c*) presents δ_3 normalised by the viscous length scale δ_ν. The normalised width, $\delta_3/\delta_\nu \approx 10$, remains nearly constant near the wall for $y^+ \lesssim 50$. Thus, the width of the mean velocity jump due to shear is governed by the viscous length scale. A corresponding scaling for Δu_3 can be obtained by assuming $\delta_3 \sim \delta_\nu$. It has been shown that shear makes a dominant contribution to the kinetic energy dissipation rate (Pirozzoli *et al.* 2010; Nagata *et al.* 2020), implying that the mean shear within shear layers scales as $|\partial \overline{u_3}/\partial \zeta_2| \sim \sqrt{\langle \varepsilon \rangle_T/\nu}$.

Combining this estimate with $\delta_3 \sim \delta_\nu$ yields the scaling

$$\Delta u_3 = \delta_3 \left| \frac{\partial \overline{u_3}}{\partial \zeta_2} \right| \sim \frac{\delta_\nu}{\tau_{\eta T}}, \tag{4.5}$$

which is the velocity scale obtained from the characteristic shear-layer thickness scale, δ_ν, and the characteristic small-scale shear time scale, $\tau_{\eta T}$. This scaling can also be rewritten as $\Delta u_3 \sim u_{\eta T}^2/u_\tau$, highlighting its difference from $\Delta u_3 \sim u_{\eta T}$ by the factor $u_{\eta T}/u_\tau$. This scaling is examined in figure 12(*d*), which plots $\Delta u_3/(\delta_\nu/\tau_{\eta T})$ against y^+. In the buffer layer, where Δu_3 does not scale with $u_{\eta T}$, $\Delta u_3/(\delta_\nu/\tau_{\eta T}) \approx 20$ remains approximately constant. This constancy is observed for $y^+ \lesssim 50$, throughout the buffer layer up to the lower edge of the logarithmic layer.

Two distinct scalings are observed depending on wall-normal location. Above $y^+ \approx 50$, the mean velocity jump and its width associated with shear scale with the Kolmogorov velocity and length scales, respectively, consistent with turbulence without wall influence, such as homogeneous isotropic turbulence and turbulent planar jets. This height, $y^+ \approx 50$, approximately corresponds to the lower edge of the logarithmic layer. These results indicate that the shear in the logarithmic and outer layers above $y^+ \approx 50$ originates from small-scale turbulent motions with scales set by the Kolmogorov scales, without direct wall influence. The approximate constancy of $\delta_3/\eta_T \approx 5$ and $\Delta u_3/u_{\eta T} \approx 8$ is also reflected in one-point statistics: since $\langle I_S \rangle_T$ scales with a characteristic shear $\Delta u_3/\delta_3$, Kolmogorov scaling of Δu_3 and δ_3 is consistent with the plateau of $\langle I_S \rangle_T/\tau_{\eta T}^{-1}$ in figure 3(*b*). The shear layer has a velocity gradient of about $(\Delta u_3/\delta_3)/\tau_{\eta T}^{-1} \approx 1.5$ at its centre, which is of the same order as $\langle I_S \rangle_T/\tau_{\eta T}^{-1} \approx 0.9$. Below $y^+ \approx 50$, namely within the buffer layer, the width of the mean velocity jump scales with the viscous length δ_ν determined by the wall shear stress, and the corresponding velocity jump follows (4.5). The present DNS yields $\delta_3/\delta_\nu \approx 10$ and $\Delta u_3/(\delta_\nu/\tau_{\eta T}) \approx 20$, which vary only weakly with y^+ for $y^+ \lesssim 50$. These values are also insensitive to Reynolds number. Although δ_3/η_T and δ_3/δ_ν for different Re_θ collapse well onto single curves in figures 12(*a*) and (*c*), their approximate constancy is observed only for $y^+ \gtrsim 50$ and $y^+ \lesssim 50$, respectively. This distinction indicates that Kolmogorov scaling governs the logarithmic and outer layers, whereas viscous scaling governs the buffer layer.

The relation between the Kolmogorov and viscous normalisations can be understood from the y^+ dependence of the Kolmogorov scales. Previous studies of TBLs showed that the Kolmogorov length in wall units, $\eta_T^+ = \eta_T/\delta_\nu$, is described approximately by a universal function of y^+ from the wall to the logarithmic layer (Stanislas *et al.* 2008; Herpin *et al.* 2013; Gustenyov *et al.* 2023). Since $u_{\eta T}^+ = u_{\eta T}/u_\tau = 1/\eta_T^+$, the Kolmogorov velocity in wall units also follows a corresponding universal relation. Thus, if δ_3/η_T and $\Delta u_3/u_{\eta T}$ are nearly constant in the logarithmic layer, then $\delta_3/\delta_\nu = (\delta_3/\eta_T)\eta_T^+$ and $\Delta u_3/(\delta_\nu/\tau_{\eta T}) = (\Delta u_3/u_{\eta T})/u_{\eta T}^+$ also become universal functions of y^+. However, this does not imply viscous scaling of δ_3 and Δu_3 in the logarithmic layer, because these normalised quantities vary significantly with y^+.

The agreement between the present TBL results and previous results for homogeneous isotropic turbulence and turbulent planar jets also indicates that the shear-layer properties in the logarithmic and outer layers are not dictated directly by large-scale features associated with turbulence generation. These features include the forcing scheme in forced isotropic turbulence and mean velocity gradients in shear flows. Thus, although the large-scale mechanisms that sustain turbulence differ among these flows, the small-scale shear layers in the logarithmic and outer layers appear to be governed primarily by the scales of small-scale motions.

Vortex tubes emerge from shear-layer roll-up and breakdown (Vincent & Meneguzzi 1994; Passot *et al.* 1995; Watanabe *et al.* 2020*b*). On the basis of this established pathway, the present scalings for the shear-layer width δ_3 and velocity jump Δu_3 suggest corresponding scalings for the diameter and azimuthal velocity of the vortex tubes generated from these layers. In particular, the near-constant values of δ_3/η_T and $\Delta u_3/u_{\eta T}$ in the logarithmic and outer layers imply that vortex-tube diameter and azimuthal velocity, when normalised by the Kolmogorov scales, are approximately independent of wall-normal position in this region. This implication is consistent with previous observations of small-scale vortex tubes in channel flows, duct flows and TBLs, where the diameter and azimuthal velocity have been reported to show similar Kolmogorov-scaled values with weak dependence on Reynolds number and flow configuration (Tanahashi *et al.* 2004; Mouri *et al.* 2004; Del Alamo *et al.* 2006; Mouri *et al.* 2007; Kang *et al.* 2007; Mouri & Hori 2009; Pirozzoli *et al.* 2008; Stanislas *et al.* 2008; Herpin *et al.* 2013). Therefore, the Kolmogorov scaling of shear layers observed here in the logarithmic and outer layers is expected to reflect a common small-scale property of wall-bounded turbulence, although direct confirmation using TDM-based analyses of other canonical wall-bounded flows remains a subject for future work. Conversely, the increase in δ_3/η_T and $\Delta u_3/u_{\eta T}$ towards the wall within the buffer layer is consistent with earlier reports of larger normalised diameter and azimuthal velocity of vortex tubes in the same region (Tanahashi *et al.* 2004).

An experiment on a TBL showed that the width of the mean velocity jump across shear layers becomes nearly independent of wall-normal position when normalised by the Taylor microscale (Eisma *et al.* 2015), as discussed in § 1. Figure 13(*a*) shows the wall-normal profile of δ_3 normalised by the Taylor microscale λ_T. Except near the wall, δ_3/λ_T exhibits little dependence on y/δ for each Reynolds number. However, the profiles do not collapse

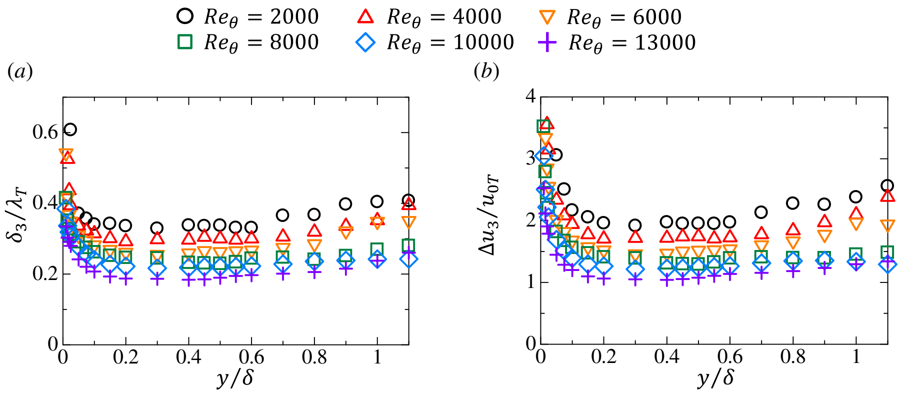

Figure 13: Wall-normal variations of (*a*) δ_3 normalised by the Taylor microscale and (*b*) Δu_3 normalised by the large-scale velocity $u_{0T} = \sqrt{(u^2_{rmsT} + v^2_{rmsT} + w^2_{rmsT})/3}$.

onto a single curve and instead vary with Re_θ. In contrast, the width normalised by η_T in figure 12(*a*) is essentially independent of Re_θ. The weak wall-normal dependence of δ_3/λ_T arises because the ratio between the Kolmogorov scale and the Taylor microscale varies only weakly with y in the outer layer for each Re_θ case. A similar issue arises for the mean velocity jump normalised by a large-scale velocity. Figure 13(*b*) shows Δu_3 normalised by u_{0T}, a characteristic velocity of large-scale motions. For each Re_θ case, $\Delta u_3/u_{0T}$ varies only weakly with wall-normal position, although it depends strongly on Re_θ. Therefore, when the length and velocity scales of shear layers are inferred from wall-normal profiles in a TBL at a fixed Re_θ, it is difficult to distinguish Kolmogorov-based scaling from alternative scalings. This issue must be addressed by examining TBLs at different Reynolds numbers.

The above comparison does not imply that the Taylor-microscale scaling reported in previous studies is incorrect. Rather, different identification procedures may emphasise different flow features. Shearing motions can exist over a wide range of scales (Watanabe *et al.* 2024; Arun *et al.* 2025; Han *et al.* 2026*b*,*a*). For example, Watanabe *et al.* (2024) examined low-pass-filtered velocity fields in high-Reynolds-number turbulence and showed that self-similar shear layers appear over a range of scales in the inertial subrange. When shear layers are identified from velocity distributions rather than from velocity gradients, the detected layers with large velocity jumps may represent larger-scale shear layers whose thicknesses are larger than the Kolmogorov scale. Such shear layers larger than the Kolmogorov scale have been reported in previous studies (Ishihara *et al.* 2013; Watanabe *et al.* 2024).

The difference from Eisma *et al.* (2015), who also used the TDM to identify the shear layers, may additionally be related to the wall-normal behaviour of the turbulence length scales. In the present DNS, λ_T/η_T varies only weakly with wall-normal position for $0.2 \lesssim y/\delta \lesssim 0.8$. Since λ_T/η_T is proportional to the square root of the turbulent Reynolds number, this behaviour is consistent with other TBL data showing that the turbulent Reynolds number Re_λ varies only weakly with y for $0.2 \lesssim y/\delta \lesssim 0.8$ at a fixed Reynolds number and streamwise position (Djenidi *et al.* 2017; Kamruzzaman *et al.* 2018). Hence, the collapse of δ_3/η_T and the weak wall-normal variation of δ_3/λ_T can appear similar at a fixed Reynolds number for $y/\delta \gtrsim 0.2$ in the present study. In contrast, the data of Eisma et al. (2015) show that the layer thickness normalised by η varies with wall-normal position, whereas that normalised by λ is nearly constant even for $y/\delta > 0.2$. This implies that λ/η also varies with wall-normal position in their data. The approximate constancy of λ/η, or equivalently Re_λ, in the outer layer has not been observed in every TBL dataset. For example, Obligado *et al.*

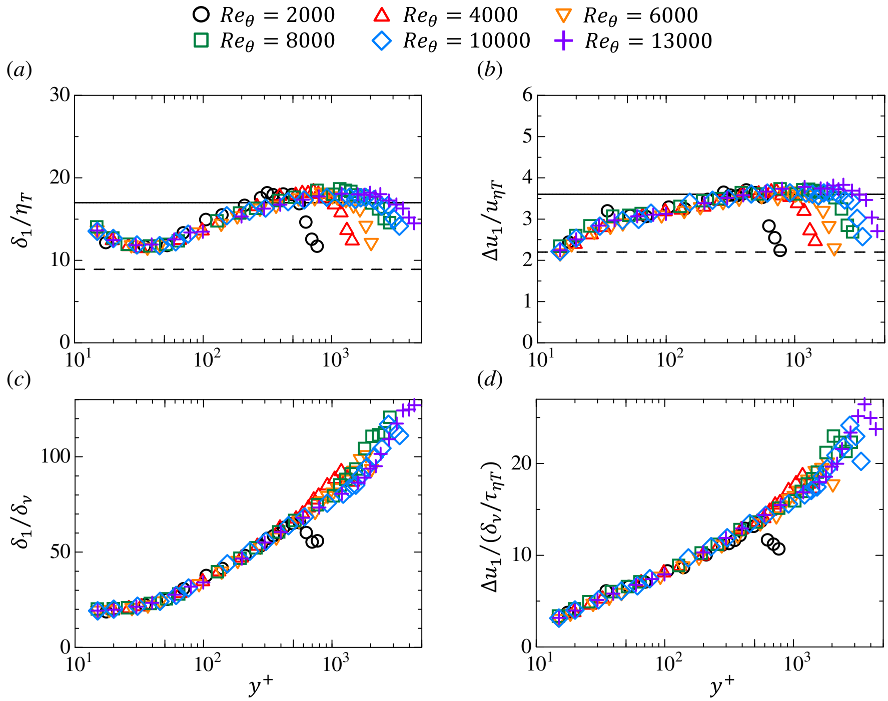

Figure 14: Wall-normal variations of (a, c) the width δ_1 and (b, d) the jump Δu_1 in the mean velocity associated with extensional strain: (a) δ_1/η_T, (b) $\Delta u_1/u_{\eta T}$, (c) δ_1/δ_ν and (d) $\Delta u_1/(\delta_\nu/\tau_{\eta T})$. In (a) and (b), horizontal lines indicate $\delta_1/\eta_T = 8.9$ and 17.0 and $\Delta u_1/u_{\eta T} = 2.2$ and 3.6, corresponding to the minimum and maximum values in transverse profiles of turbulent planar jets (Hayashi *et al.* 2021*a*).

(2022) reported wall-normal variations of Re_λ in the range $0.4 < y/\delta < 0.8$ for different Re_θ cases. Some cases exhibit only weak variations of Re_λ with y/δ, whereas others show an increase in Re_λ with y/δ. The different conclusion on the y/δ dependence in Eisma et al. (2015) may therefore reflect not only the type of detected shear layer, but also differences in the wall-normal behaviour of the turbulence length scales.

4.4. *Mean velocity jump associated with strain*

Mean velocity jumps are also observed due to large $\partial\overline{u_1}/\partial\zeta_1$ and $\partial\overline{u_2}/\partial\zeta_2$, which are associated with extension and compression in the biaxial strain, respectively. The mean velocity jumps for these components are examined below.

Figure 14 shows wall-normal variations of δ_1 and Δu_1 with normalisations based on η_T and δ_ν and the corresponding velocity scales, $u_{\eta T}$ and $\delta_\nu/\tau_{\eta T}$, as also used for δ_3 and Δu_3. In figures 14(a) and (b), the ranges $\delta_1/\eta_T = 8.9$–17.0 and $\Delta u_1/u_{\eta T} = 2.2$–$3.6$ reported from DNS of turbulent planar jets are indicated by horizontal lines (Hayashi *et al.* 2021*a*). These variations in jets arise mainly from transverse-position dependence rather than Reynolds-number effects. Wall-normal variations of δ_1/η_T and $\Delta u_1/u_{\eta T}$ for $y^+ \gtrsim 50$ are more pronounced than those of δ_3 and Δu_3, for which Kolmogorov scaling is observed. Except near the TBL edge, δ_1/η_T and $\Delta u_1/u_{\eta T}$ collapse well onto single curves for $y^+ \gtrsim 50$, and the magnitude of the wall-normal variation, $\delta_1/\eta_T \approx 11$–$19$ and $\Delta u_1/u_{\eta T} \approx 3.0$–$3.8$, lies within the range reported for the turbulent planar jets. In the jets, δ_1/η_T and $\Delta u_1/u_{\eta T}$ decrease towards the jet edge, and a similar trend is observed towards the edge of the TBL.

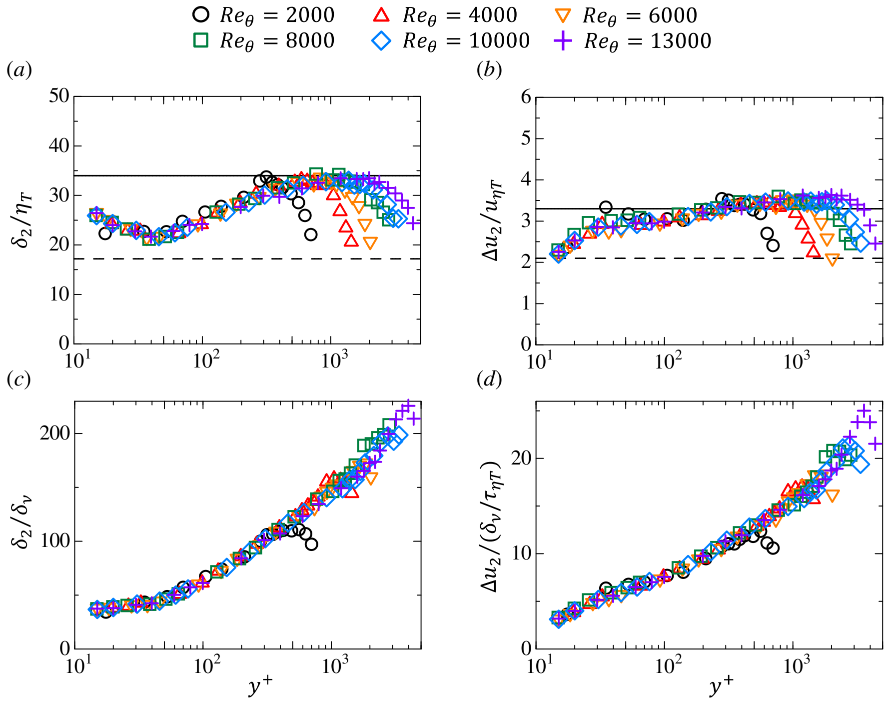

Figure 15: The same as figure 14, but for δ_2 and Δu_2: (*a*) δ_2/η_T, (*b*) $\Delta u_2/u_{\eta T}$, (*c*) δ_2/δ_ν and (*d*) $\Delta u_2/(\delta_\nu/\tau_{\eta T})$. In (*a*) and (*b*), horizontal lines indicate $\delta_2/\eta_T = 17.2$ and 34.0 and $\Delta u_2/u_{\eta T} = 2.1$ and 3.3, corresponding to the minimum and maximum values in transverse profiles of turbulent planar jets (Hayashi *et al.* 2021*a*).

Figures 14(*c*) and (*d*) examine viscous-length scaling for δ_1 and Δu_1 by normalising them with δ_ν and $\delta_\nu/\tau_{\eta T}$, respectively. As the wall is approached, δ_1/δ_ν tends towards an approximately constant value of about 19. In contrast, $\Delta u_1/(\delta_\nu/\tau_{\eta T})$ decreases continuously towards the wall.

Figure 15 presents the results for δ_2 and Δu_2. Figures 15(*a*) and (*b*) show wall-normal variations of $\delta_2/\eta_T \approx 21$–34 and $\Delta u_2/u_{\eta T} \approx 2.9$–3.6 in the TBLs, compared with the ranges $\delta_2/\eta_T = 17.2$–34.0 and $\Delta u_2/u_{\eta T} = 2.1$–3.3 (horizontal lines) obtained from DNS of turbulent planar jets (Hayashi *et al.* 2021*a*). The wall-normal variations are similar to those of δ_1/η_T and $\Delta u_1/u_{\eta T}$. Both δ_2/η_T and $\Delta u_2/u_{\eta T}$ vary with y for $y^+ \gtrsim 50$ by amounts comparable to those in jets, whereas δ_3/η_T and $\Delta u_3/u_{\eta T}$ are nearly constant in the same region. Figures 15(*c*) and (*d*) show δ_2/δ_ν and $\Delta u_2/(\delta_\nu/\tau_{\eta T})$. As for δ_1 and Δu_1, $\delta_2/\delta_\nu \approx 37$ becomes nearly independent of y^+ and Re_θ near the wall, while $\Delta u_2/(\delta_\nu/\tau_{\eta T})$ continues to decrease towards the wall.

The mean velocity jumps associated with strain exhibit wall-normal variations in δ_i/η_T and $\Delta u_i/u_{\eta T}$ $(i = 1, 2)$. Figures 16 and 17 present δ_i/η_T and $\Delta u_i/u_{\eta T}$ $(i = 1, 2)$ as functions of y normalised by the boundary-layer thickness δ. The profiles are similar across all Re_θ cases. These wall-normal variations indicate an influence of large-scale motions on the strain acting on small-scale shear layers. The y dependence of δ_i/η_T and $\Delta u_i/u_{\eta T}$ for strain is also similar to that in jets, with both decreasing towards the edges of the TBL and jets (Hayashi *et al.* 2021*a*). This behaviour is likely related to mean-shear effects in turbulence bounded by a non-turbulent external flow.

In the buffer layer, the velocity jumps of shear layers scale differently from those in the

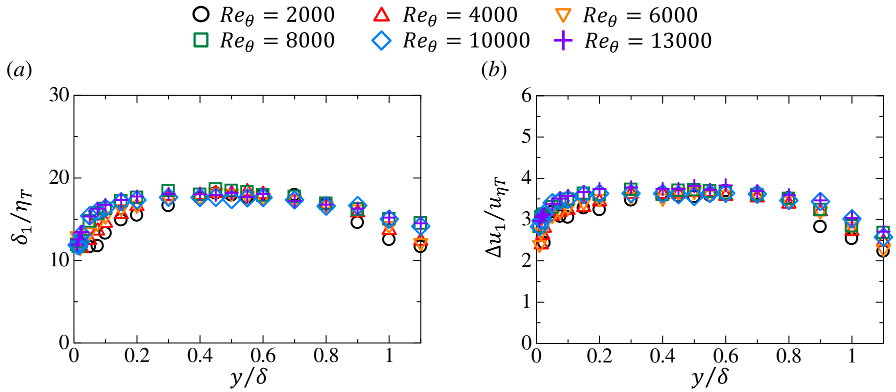

Figure 16: (*a*) δ_1/η_T and (*b*) $\Delta u_1/u_{\eta T}$ plotted against y/δ.

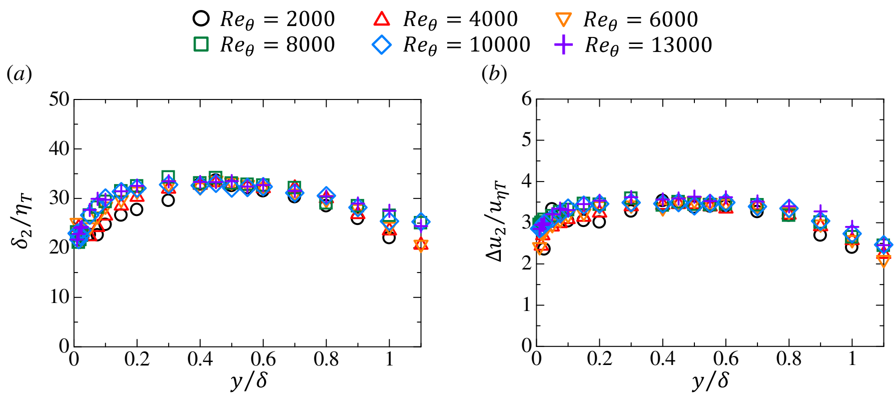

Figure 17: (*a*) δ_2/η_T and (*b*) $\Delta u_2/u_{\eta T}$ plotted against y/δ.

logarithmic and outer layers. The widths of the mean velocity jumps, normalised by the viscous length, approach constant values for both shear and strain. However, $\Delta u_1/(\delta_\nu/\tau_{\eta T})$ and $\Delta u_2/(\delta_\nu/\tau_{\eta T})$ decrease continuously towards the wall. The scaling $\delta_\nu/\tau_{\eta T}$ assumes that energy dissipation is dominated by the velocity gradient associated with the mean velocity jump across shear layers. However, Δu_1 and Δu_2 are associated with the irrotational strain components $\partial u_1/\partial \zeta_1$ and $\partial u_2/\partial \zeta_2$. Such strain contributes little to the energy dissipation, which is instead dominated by shear (Nagata *et al.* 2020). This explains why $\delta_\nu/\tau_{\eta T}$ does not govern Δu_1 and Δu_2 in the buffer layer.

4.5. *Characteristics of individual shear layers*

In addition to the velocity jumps and widths inferred from the mean velocity profiles around shear layers, local shear-layer properties are examined using probability density functions of shear-layer characteristics. We consider the local thickness and velocity jump of each shear layer, estimated from the profiles of I_S and u_3 along the ζ_2 axis, namely $I_S(0,\zeta_2,0)$ and $u_3(0,\zeta_2,0)$, following Watanabe & Nagata (2023). The shear-layer thickness δ_S is defined as the half-width of I_S. The velocity jump across the shear layer, Δu_S, is evaluated as $\Delta u_S = \delta_S(\partial u_3/\partial \zeta_2)$, where $\partial u_3/\partial \zeta_2$ is taken at the shear-layer centre. The shear Reynolds number is defined as $Re_S = \Delta u_S \delta_S/\nu$, which is relevant to the instability of each shear layer.

The same definitions were used in our shear-layer analysis of homogeneous isotropic

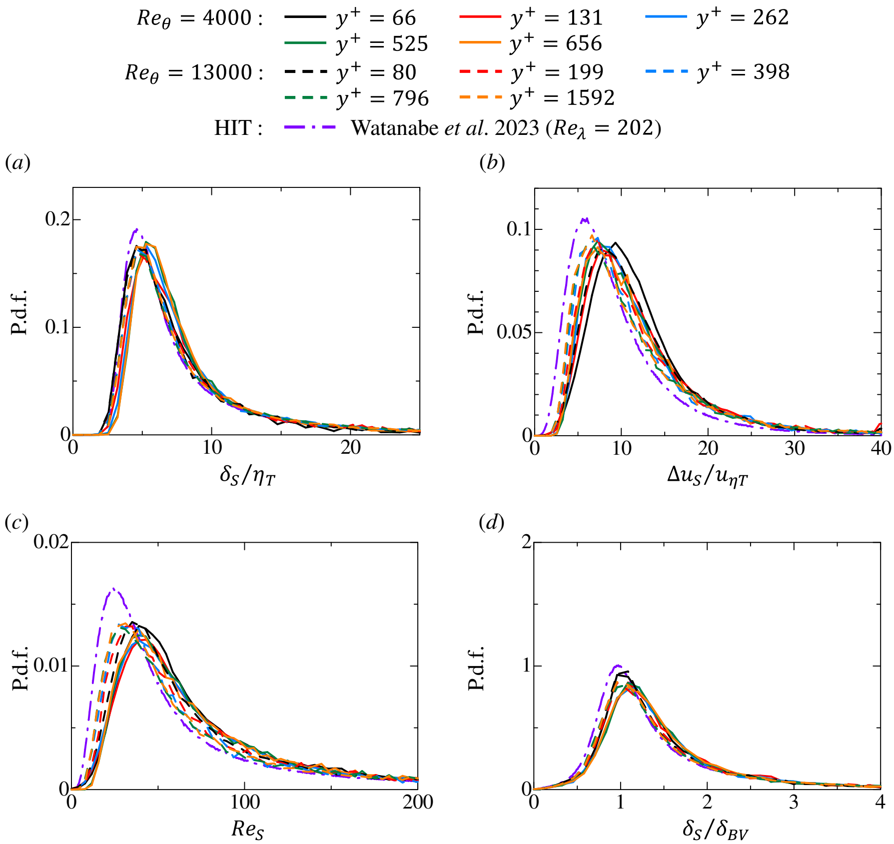

Figure 18: Probability density functions of (*a*) δ_S/η_T, (*b*) $\Delta u_S/u_{\eta T}$, (*c*) Re_S and (*d*) δ_S/δ_{BV} obtained for $y^+ > 50$ in the cases with $Re_\theta = 4000$ and 13000. Results for homogeneous isotropic turbulence (HIT) are shown for comparison (Watanabe & Nagata 2023).

turbulence (Watanabe & Nagata 2023), which is compared with the present results. The relation between shear and strain within a shear layer is consistent with Burgers' vortex layer, an exact steady solution of the Navier–Stokes equations (Burgers 1948; Davidson 2004). The thickness of Burgers' vortex layer, defined as the half-width of I_S, is related to the strain rate α as $\delta_{BV} = 1.67\sqrt{2\nu/\alpha}$. Burgers' vortex layer has a constant thickness because thickening due to viscous vorticity diffusion is balanced by compression due to biaxial strain. For each detected shear layer, the effective strain rate contributing to vortex stretching is evaluated as $\alpha = \omega_i S_{ij}\omega_j/(\omega_k\omega_k)$ at $(\zeta_1, \zeta_2, \zeta_3) = (0, 0, 0)$, and the corresponding Burgers-layer thickness δ_{BV} is compared with the actual thickness obtained from the half-width of I_S. This evaluation of α follows previous studies on vortex tubes (Jiménez & Wray 1998; da Silva *et al.* 2011).

Figures 18(*a*) and (*b*) show the p.d.f.s of δ_S and Δu_S evaluated for $y^+ > 50$ in the cases with $Re_\theta = 4000$ and 13000. In this region, the mean velocity jump associated with shear scales with the Kolmogorov scales. Accordingly, δ_S and Δu_S are normalised by η_T and $u_{\eta T}$, respectively. The present results are compared with those in homogeneous isotropic turbulence (Watanabe & Nagata 2023). The p.d.f.s of δ_S/η_T and $\Delta u_S/u_{\eta T}$ have similar distributions regardless of $y^+ > 50$ location and Re_θ, and they are also consistent with

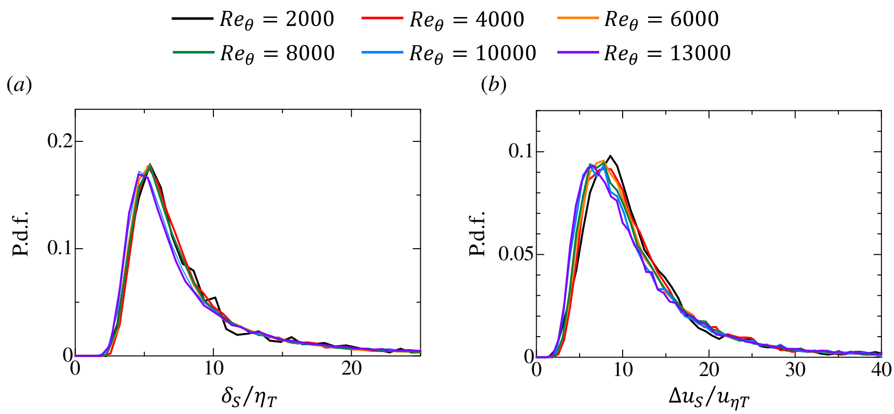

Figure 19: Probability density functions of (*a*) δ_S/η_T and (*b*) $\Delta u_S/u_{\eta T}$ at y/δ = 0.2 for all Reynolds number cases.

homogeneous isotropic turbulence. The Kolmogorov-based scalings, examined using the mean velocity profiles, therefore apply even to individual shear layers. In particular, the peaks of the p.d.f.s occur at $\delta_S/\eta_T \approx 5$ and $\Delta u_S/u_{\eta T} \approx 8$.

Figure 18(*c*) shows the p.d.f. of Re_S for the same locations and Reynolds numbers as in figures 18(*a*) and (*b*). The p.d.f. peaks at $Re_S \approx 40$. This value is consistent with the peaks at $\delta_S/\eta_T \approx 5$ and $\Delta u_S/u_{\eta T} \approx 8$, since Re_S can be written as $Re_S = (\Delta u_S/u_{\eta T})(\delta_S/\eta_T)$. Almost all shear layers satisfy $Re_S \gg 1$, indicating that Re_S is sufficiently large for shear layers to become unstable, as suggested by numerical studies of Burgers' vortex layers and strained shear layers with finite aspect ratio (Beronov & Kida 1996; Watanabe & Nagata 2023).

Figure 18(*d*) shows the p.d.f. of δ_S/δ_{BV}, examining the relation between strain and thickness in Burgers' vortex layer. The p.d.f. exhibits a pronounced peak at $\delta_S/\delta_{BV} \approx 1$ for all Re_θ and wall-normal locations. Thus, the shear-layer thickness is well predicted by the strain–thickness relation of Burgers' vortex layer.

Figure 19 presents the p.d.f.s of δ_S/η_T and $\Delta u_S/u_{\eta T}$ at a fixed wall-normal position, $y/\delta = 0.2$, for all Re_θ cases. At this wall-normal position, the p.d.f.s show only weak dependence on Re_θ. The remaining variation in the peak positions is comparable to that observed for the p.d.f.s at different y^+ in figure 18. These results indicate that the imperfect collapse of the p.d.f.s in figure 18 is not solely caused by wall-normal dependence, because a comparable level of variation remains even at fixed y/δ. Although the p.d.f.s in figures 18 and 19 do not collapse perfectly, the variation of their peak positions is limited. The peak of δ_S/η_T varies approximately between 4.6 and 5.3, and that of $\Delta u_S/u_{\eta T}$ varies between 6.6 and 9.3. These variations are small compared with the full widths of the p.d.f.s, and the peak positions remain similar for different wall-normal positions and Reynolds numbers. Comparable variations have also been reported for vortex tubes, whose radius and azimuthal velocity depend only weakly on flow type and Reynolds number. For example, previous studies reported p.d.f. peak values of the vortex-tube radius and azimuthal velocity with variations comparable to those observed here for δ_S/η_T and $\Delta u_S/u_{\eta T}$ (Tanahashi *et al.* 2001; Kang *et al.* 2007).

Figures 20(*a*) and (*b*) show the p.d.f.s of δ_S/δ_ν and $\Delta u_S/(\delta_\nu/\tau_{\eta T})$ in the buffer layer, where δ_ν characterises the mean velocity profile associated with shear. The p.d.f.s exhibit peaks at $\delta_S/\delta_\nu \approx 8$ and $\Delta u_S/(\delta_\nu/\tau_{\eta T}) \approx 20$ at the examined wall-normal locations, largely independent of Re_θ. The distribution of $\Delta u_S/(\delta_\nu/\tau_{\eta T})$ broadens as y^+ increases, indicating

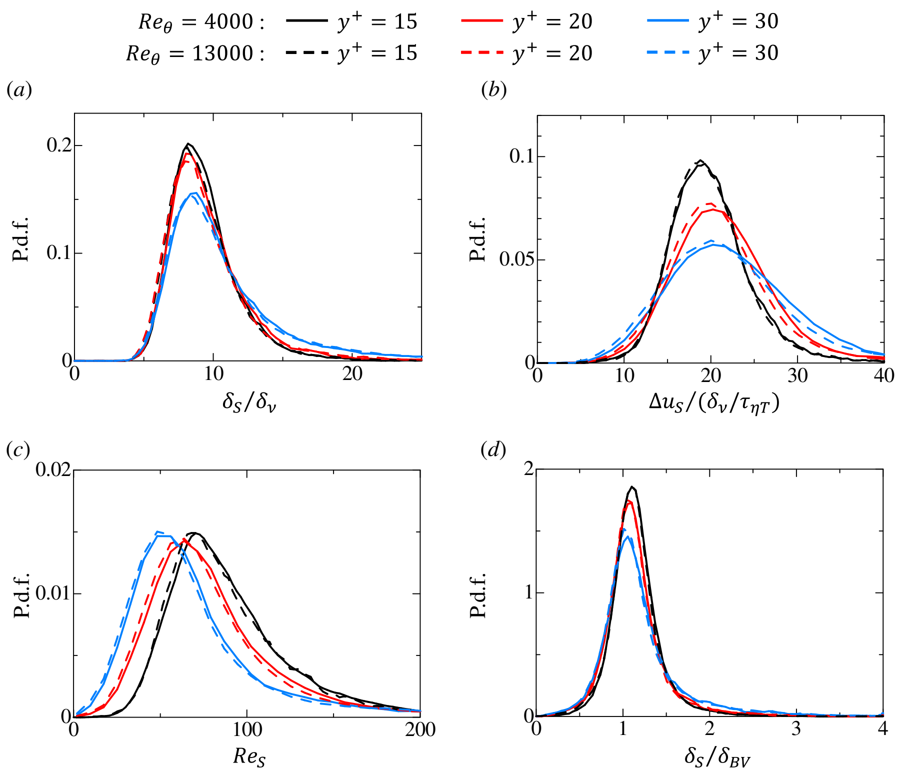

Figure 20: The same as figure 18, but for $y^+ < 50$.

that fluctuations in shear-layer characteristics become larger away from the wall. Figure 20(*c*) shows the p.d.f. of Re_S. From $y^+ = 30$ to 15, the p.d.f. of Re_S shifts towards larger Re_S values, indicating that shear layers have larger Reynolds numbers closer to the wall. Figure 20(*d*) shows the p.d.f. of δ_S/δ_{BV}. The peak at $\delta_S/\delta_{BV} \approx 1$ confirms a balance between strain and viscous diffusion similar to that in Burgers' vortex layer. The p.d.f. for $y^+ < 50$ is narrower than that for $y^+ > 50$, and deviations from this balanced state occur more frequently for $y^+ > 50$, where shear-layer characteristics are set by the Kolmogorov scales.

These scalings of δ_S and Δu_S are directly relevant to flow-control strategies that leverage small-scale shear instability (Watanabe & Nagata 2023; Watanabe 2024; Watanabe & Nagata 2025). The most effective perturbation wavelength for exciting this instability scales with the shear-layer thickness. The perturbation effectiveness is also governed by the imposed disturbance energy normalised by the square of the shear-layer velocity jump. Thus, the present two-regime scaling provides a basis for estimating both the instability wavelength and the disturbance intensity required to destabilise small-scale shear layers in wall turbulence. Specifically, the unstable wavelength is about $7\delta_S$ (Watanabe & Nagata 2023), which can be expressed as approximately $36\eta_T$ in the logarithmic and outer layers and $60\delta_\nu$ in the buffer layer based on the peaks in the p.d.f.s of δ_S. The corresponding velocity scale is $u_{\eta T}$ in the logarithmic and outer layers and $\delta_\nu/\tau_{\eta T}$ in the buffer layer. These estimates clarify how disturbance parameters should be selected differently in the buffer layer and in the logarithmic or outer layers.

5. Conclusion

The scalings of small-scale shear layers are investigated using DNS databases of temporally developing TBLs with the Reynolds number based on momentum thickness, Re_θ, ranging from 2000 to 13000. Shear layers are identified as regions of locally intense shear using the TDM of the velocity gradient tensor. Conditional averages are evaluated in a local shear coordinate system in order to observe shear layers in a common reference frame aligned with their orientations. Shear-layer characteristics are examined for different Re_θ and wall-normal positions from the buffer layer to the outer layer.

Mean flow profiles around shear layers confirm that shear layers form within a biaxial strain field, in which shear vorticity is stretched and the shear layer is compressed in the layer-normal direction. This shear–strain relation, previously observed in homogeneous isotropic turbulence and turbulent planar jets, persists even near the wall. Shear-layer orientation is influenced by the wall: shear layers near the wall tend to be parallel to it. Although this trend is also observed in the logarithmic and outer layers, shear layers exhibit a range of orientations, and the local shear does not necessarily align with the mean shear.

Conditional averaging around near-wall shear layers reveals two distinct regions of intense rigid-body rotation on the wall side of the shear layer. Their coupling with the shear layer near the wall contributes to the Reynolds stress through the transfer of shear-related streamwise momentum by the wall-normal non-shear velocity component. This mechanism is consistent with counter-rotating vortex pairs in wall turbulence.

The mean velocity jump of shear across the layer, Δu_3, and its width, δ_3, are examined as functions of y and Re_θ. For $y^+ \gtrsim 50$ in the logarithmic and outer layers, δ_3 and Δu_3 scale with the Kolmogorov length η_T and the Kolmogorov velocity $u_{\eta T}$, respectively. Specifically, the present DNS yields $\delta_3/\eta_T \approx 5$ and $\Delta u_3/u_{\eta T} \approx 8$. For $y^+ \lesssim 50$, mostly in the buffer layer, δ_3 scales with the viscous length δ_ν of wall turbulence. Assuming that shear dominates the kinetic energy dissipation, $\delta_3 \sim \delta_\nu$ leads to $\Delta u_3 \sim \delta_\nu/\tau_{\eta T}$, which is supported by the present data. The DNS yields $\delta_3/\delta_\nu \approx 10$ and $\Delta u_3/(\delta_\nu/\tau_{\eta T}) \approx 20$ for all Re_θ values.

The mean velocity jumps and widths associated with the biaxial strain also exhibit Kolmogorov-based scaling for $y^+ \gtrsim 50$. The normalised jumps and widths depend only weakly on Re_θ, but vary with wall-normal position. In the logarithmic and outer layers, the present results yield $\delta_1/\eta_T \approx 11$–$19$ and $\Delta u_1/u_{\eta T} \approx 3.0$–$3.8$ for the extensional strain, and $\delta_2/\eta_T \approx 21$–$34$ and $\Delta u_2/u_{\eta T} \approx 2.9$–$3.6$ for the compressive strain. The wall-normal variations of the mean velocity jumps associated with biaxial strain collapse when plotted against y/δ, indicating the influence of large-scale motions on the strain. In the buffer layer, $\delta_1/\delta_\nu \approx 19$ and $\delta_2/\delta_\nu \approx 37$ become nearly independent of y^+ and Re_θ. However, the scaling based on $\delta_\nu/\tau_{\eta T}$ does not apply to the corresponding velocity jumps, because biaxial strain contributes little to the energy dissipation.

The p.d.f.s of shear-layer thickness and shear-related velocity jump support the above scalings for individual shear layers. The Reynolds number of almost all shear layers is sufficiently large for the layers to be unstable, regardless of wall-normal position. The shear-layer thickness is also close to the estimate based on Burgers' vortex layer even near the wall, indicating a balance between thickening due to viscous vorticity diffusion and compression due to biaxial strain.

The shear-layer characteristics for $y^+ \gtrsim 50$ are consistent with previous studies of turbulent planar jets (Hayashi *et al.* 2021*a*). The mean velocity jumps and widths for all components agree quantitatively with DNS data of turbulent planar jets. In addition, the normalised mean velocity jumps and widths decrease towards the TBL edge, consistent with shear-layer behaviour near the jet edge. These results indicate negligible direct wall influence on shear layers in the logarithmic and outer layers.

The present study establishes two distinct scalings of small-scale shear layers in TBLs. These scalings provide a basis for estimating shear-layer properties using turbulence length scales defined from conventional velocity statistics. Such estimates are crucial for testing and applying flow-control strategies that leverage the instability of small-scale shear layers, which has been shown to enhance turbulent mixing and entrainment in wall-free turbulent flows.

Acknowledgements. The numerical simulations were performed using the high-performance computing systems at the Japan Agency for Marine-Earth Science and Technology and Nagoya University. This work was also supported by a Collaborative Research Project on Computer Science with High-Performance Computing in Nagoya University. The authors used ChatGPT, an AI language model developed by OpenAI and accessed through the ChatGPT web application in 2026, to assist with English-language editing and to improve grammar, spelling and clarity. All AI-assisted edits were reviewed and approved by the authors, who take full responsibility for the content of the manuscript.

Funding. This work was supported by JSPS KAKENHI Grant Nos. JP23K22669, JP25K01155, and JP26K22434 and JST SPRING Grant No. JPMJSP2110.

Declaration of interests. The authors report no conflicts of interest.

Data availability statement. The data supporting the findings of this study are available from the corresponding author upon reasonable request.

REFERENCES

Adrian, R. J., Meinhart, C. D. & Tomkins, C. D. 2000 Vortex organization in the outer region of the turbulent boundary layer. *J. Fluid Mech.* **422**, 1–54.

Arun, R. & Colonius, T. 2024 Velocity gradient partitioning in turbulent flows. *J. Fluid Mech.* **1000**, R5.

Arun, R., Kamal, M., Colonius, T. & Johnson, P. L. 2025 Normality-based analysis of multiscale velocity gradients and energy transfer in direct and large-eddy simulations of isotropic turbulence. *J. Fluid Mech.* **1021**, A47.

Bakewell Jr., H. P. & Lumley, J. L. 1967 Viscous sublayer and adjacent wall region in turbulent pipe flow. *Phys. Fluids* **10** (9), 1880–1889.

Baldyga, J. & Pohorecki, R. 1995 Turbulent micromixing in chemical reactors–a review. *The Chem. Engng. J. & the Biochem. Engng. J.* **58** (2), 183–195.

Beronov, K. N. & Kida, S. 1996 Linear two-dimensional stability of a Burgers vortex layer. *Phys. Fluids* **8** (4), 1024–1035.

Blackwelder, R. F. & Eckelmann, H. 1979 Streamwise vortices associated with the bursting phenomenon. *J. Fluid Mech.* **94** (3), 577–594.

Blocken, B., Stathopoulos, T.ed, Saathoff, P & Wang, X 2008 Numerical evaluation of pollutant dispersion in the built environment: comparisons between models and experiments. *J. Wind Eng. Ind. Aerodyn.* **96** (10-11), 1817–1831.

Burgers, J. M. 1948 A mathematical model illustrating the theory of turbulence. *Adv. Appl. Mech.* **1**, 171–199.

Chen, X., Chung, Y. M. & Wan, M. 2021 The uniform-momentum zones and internal shear layers in turbulent pipe flows at Reynolds numbers up to $re_\tau = 1000$. *Int. J. Heat Fluid Flow* **90**, 108817.

Chillà, F. & Schumacher, J. 2012 New perspectives in turbulent Rayleigh-Bénard convection. *Eur. Phys. J. E.* **35** (7), 58.

Das, R. & Girimaji, S. S. 2020 Revisiting turbulence small-scale behavior using velocity gradient triple decomposition. *New J. Phys.* **22** (6), 063015.

Davidson, P. A. 2004 *Turbulence: An Introduction for Scientists and Engineers*. Oxford Univ. Pr.

De Graaff, D. B. & Eaton, J. K. 2000 Reynolds-number scaling of the flat-plate turbulent boundary layer. *J. Fluid Mech.* **422**, 319–346.

De Silva, C. M., Philip, J., Hutchins, N. & Marusic, I. 2017 Interfaces of uniform momentum zones in turbulent boundary layers. *J. Fluid Mech.* **820**, 451–478.

Del Alamo, J. C., Jiménez, J., Zandonade, P. & Moser, R. D. 2006 Self-similar vortex clusters in the turbulent logarithmic region. *J. Fluid Mech.* **561**, 329–358.

Djenidi, L., Antonia, R. A., Talluru, M. K. & Abe, H. 2017 Skewness and flatness factors of the longitudinal velocity derivative in wall-bounded flows. *Phys. Rev. Fluids* **2** (6), 064608.

Driscoll, J. F. 2008 Turbulent premixed combustion: Flamelet structure and its effect on turbulent burning velocities. *Prog. Energy Combust. Sci.* **34** (1), 91–134.

Eisma, J., Westerweel, J., Ooms, G. & Elsinga, G. E. 2015 Interfaces and internal layers in a turbulent boundary layer. *Phys. Fluids* **27** (5), 055103.

Enoki, R., Watanabe, T. & Nagata, K. 2023 Statistical properties of shear and nonshear velocity components in isotropic turbulence and turbulent jets. *Phys. Rev. Fluids* **8** (10), 104602.

Fan, D., Xu, J., Yao, M. X. & Hickey, J.-P. 2019 On the detection of internal interfacial layers in turbulent flows. *J. Fluid Mech.* **872**, 198–217.

Fiscaletti, D., Buxton, O. R. H. & Attili, A. 2021 Internal layers in turbulent free-shear flows. *Phys. Rev. Fluids* **6** (3), 034612.

Ganapathisubramani, B., Lakshminarasimhan, K. & Clemens, N. T. 2008 Investigation of three-dimensional structure of fine scales in a turbulent jet by using cinematographic stereoscopic particle image velocimetry. *J. Fluid Mech.* **598**, 141–175.

Ghira, A. A., Elsinga, G. E. & da Silva, C. B. 2022 Characteristics of the intense vorticity structures in isotropic turbulence at high Reynolds numbers. *Phys. Rev. Fluids* **7** (10), 104605.

Goto, S., Saito, Y. & Kawahara, G. 2017 Hierarchy of antiparallel vortex tubes in spatially periodic turbulence at high Reynolds numbers. *Phys. Rev. Fluids* **2** (6), 064603.

Gul, M., Elsinga, G. E. & Westerweel, J. 2020 Internal shear layers and edges of uniform momentum zones in a turbulent pipe flow. *J. Fluid Mech.* **901**, A10.

Gustenyov, N., Egerer, M., Hultmark, M., Smits, A. J. & Bailey, S. C. C. 2023 Similarity of length scales in high-Reynolds-number wall-bounded flows. *J. Fluid Mech.* **965**, A17.

Han, Z., Sakai, H., Watanabe, T. & Nagata, K. 2026*a* Shear-layer structures in turbulence generated by opposed multiple-fan arrays. *Int. Commun. Heat Mass Transf.* **179**, 112209.

Han, Z., Watanabe, T. & Nagata, K. 2026*b* Scale-dependent characteristics of shear layers in turbulence subject to axisymmetric expansion. *Phys. Fluids* **38** (8).

Hayashi, M., Watanabe, T. & Nagata, K. 2021*a* Characteristics of small-scale shear layers in a temporally evolving turbulent planar jet. *J. Fluid Mech.* **920**, A38.

Hayashi, M., Watanabe, T. & Nagata, K. 2021*b* The relation between shearing motions and the turbulent/non-turbulent interface in a turbulent planar jet. *Phys. Fluids* **33** (5), 055126.

Hearst, R. J., de Silva, C. M., Dogan, E. & Ganapathisubramani, B. 2021 Uniform-momentum zones in a turbulent boundary layer subjected to freestream turbulence. *J. Fluid Mech.* **915**, A109.

Herpin, S., Stanislas, M., Foucaut, J. M. & Coudert, S. 2013 Influence of the Reynolds number on the vortical structures in the logarithmic region of turbulent boundary layers. *Journal of Fluid Mechanics* **716**, 5–50.

Ho, C.-M. & Huerre, P. 1984 Perturbed free shear layers. *Annu. Rev. Fluid Mech.* **16**, 365–424.

Holmes, P., Lumley, J. L., Berkooz, G. & Rowley, C. W. 2012 *Turbulence, coherent structures, dynamical systems and symmetry*. Cambridge university press.

Ishihara, T., Kaneda, Y. & Hunt, J. C. R. 2013 Thin shear layers in high Reynolds number turbulence–DNS results. *Flow, Turbul. Combust.* **91** (4), 895–929.

Jahanbakhshi, R., Vaghefi, N. S. & Madnia, C. K. 2015 Baroclinic vorticity generation near the turbulent/non-turbulent interface in a compressible shear layer. *Phys. Fluids* **27** (10), 105105.

Jiménez, J. & Wray, A. A. 1998 On the characteristics of vortex filaments in isotropic turbulence. *J. Fluid Mech.* **373**, 255–285.

Jiménez, J., Wray, A. A., Saffman, P. G. & Rogallo, R. S. 1993 The structure of intense vorticity in isotropic turbulence. *J. Fluid Mech.* **255**, 65–90.

Johnson, P. L. & Wilczek, M. 2024 Multiscale velocity gradients in turbulence. *Annu. Rev. Fluid Mech.* **56** (1), 463–490.

Kamruzzaman, M., Djenidi, L. & Antonia, R. A. 2018 Behaviour of the energy dissipation coefficient in a rough wall turbulent boundary layer. *Exp. Fluids* **59** (1), 9.

Kang, S.-J., Tanahashi, M. & Miyauchi, T. 2007 Dynamics of fine scale eddy clusters in turbulent channel flows. *J. Turbul.* **8**, N52.

Kida, S. & Miura, H. 1998 Identification and analysis of vortical structures. *Eur. J. Mech. B* **17** (4), 471–488.

Kolář, V. 2007 Vortex identification: New requirements and limitations. *Int. J. Heat Fluid Flow* **28** (4), 638–652.

Kozul, M., Chung, D. & Monty, J. P. 2016 Direct numerical simulation of the incompressible temporally developing turbulent boundary layer. *J. Fluid Mech.* **796**, 437–472.

Marusic, I., Monty, J. P., Hultmark, M. & Smits, A. J. 2013 On the logarithmic region in wall turbulence. *J. Fluid Mech.* **716**, R3.

Meinhart, C. D. & Adrian, R. J. 1995 On the existence of uniform momentum zones in a turbulent boundary layer. *Phys. Fluids* **7** (4), 694–696.

Mouri, H. & Hori, A. 2009 Vortex tubes in turbulence velocity fields at high Reynolds numbers. *Fluid Dyn. Res.* **41** (2), 021402.

Mouri, H., Hori, A. & Kawashima, Y. 2004 Vortex tubes in turbulence velocity fields at Reynolds numbers re_λ $simeq300 - -1300$. *Phys. Rev. E* **70** (6), 066305.

Mouri, H., Hori, A. & Kawashima, Y. 2007 Laboratory experiments for intense vortical structures in turbulence velocity fields. *Phys. Fluids* **19** (5), 055101.

Nagata, R., Watanabe, T., Nagata, K. & da Silva, C. B. 2020 Triple decomposition of velocity gradient tensor in homogeneous isotropic turbulence. *Comput. Fluids* **198**, 104389.

Obligado, M., Brun, C., Silvestrini, J. H. & Schettini, E. B. C. 2022 Dissipation scalings in the turbulent boundary layer at moderate re_θ. *Flow, Turbul. Combust.* **108** (1), 105–122.

Passot, T., Politano, H., Sulem, P. L., Angilella, J. R. & Meneguzzi, M. 1995 Instability of strained vortex layers and vortex tube formation in homogeneous turbulence. *J. Fluid Mech.* **282**, 313–338.

Pirozzoli, S., Bernardini, M. & Grasso, F. 2008 Characterization of coherent vortical structures in a supersonic turbulent boundary layer. *J. Fluid Mech.* **613**, 205–231.

Pirozzoli, S., Bernardini, M. & Grasso, F. 2010 On the dynamical relevance of coherent vortical structures in turbulent boundary layers. *J. Fluid Mech.* **648**, 325–349.

Pope, S. B. 2000 *Turbulent Flows*. Cambridge Univ. Pr.

Robinson, S. K. 1991 Coherent motions in the turbulent boundary layer. *Annu. Rev. Fluid Mech.* **23** (1), 601–639.

Ruetsch, G. R. & Maxey, M. R. 1991 Small-scale features of vorticity and passive scalar fields in homogeneous isotropic turbulence. *Phys. Fluids* **3** (6), 1587–1597.

Sillero, J. A., Jiménez, J. & Moser, R. D. 2013 One-point statistics for turbulent wall-bounded flows at reynolds numbers up to $\delta^+ \approx 2000$. *Phys. Fluids* **25** (10).

da Silva, C. B., Dos Reis, R. J. N. & Pereira, J. C. F. 2011 The intense vorticity structures near the turbulent/non-turbulent interface in a jet. *J. Fluid Mech.* **685**, 165–190.

da Silva, C. B., Hunt, J. C. R., Eames, I. & Westerweel, J. 2014 Interfacial layers between regions of different turbulence intensity. *Annu. Rev. Fluid Mech.* **46**, 567–590.

de Silva, C. M., Hutchins, N. & Marusic, I. 2016 Uniform momentum zones in turbulent boundary layers. *J. Fluid Mech.* **786**, 309–331.

Stanislas, M., Perret, L. & Foucaut, J.-M. 2008 Vortical structures in the turbulent boundary layer: a possible route to a universal representation. *J. Fluid Mech.* **602**, 327–382.

Tanahashi, M., Iwase, S. & Miyauchi, T. 2001 Appearance and alignment with strain rate of coherent fine scale eddies in turbulent mixing layer. *J. Turbulence* **2** (6), 1–18.

Tanahashi, M., Kang, S.-J., Miyamoto, T., Shiokawa, S. & Miyauchi, T. 2004 Scaling law of fine scale eddies in turbulent channel flows up to $re_\tau = 800$. *Int. J. Heat Fluid Flow* **25** (3), 331–340.

Tang, S. L. & Antonia, R. A. 2022 Scaling of small-scale wall turbulence. *J. Fluid Mech.* **948**, A25.

Tsinober, A. 2009 *An informal conceptual introduction to turbulence*. Springer.

Vincent, A. & Meneguzzi, M. 1994 The dynamics of vorticity tubes in homogeneous turbulence. *J. Fluid Mech.* **258**, 245–254.

Watanabe, T. 2024 Efficient enhancement of turbulent entrainment by small-scale shear instability. *J. Fluid Mech.* **988**, A20.

Watanabe, T., Abreu, H., Nagata, K. & da Silva, C. B. 2025 Small-scale shear layers in isotropic turbulence of viscoelastic fluids. *J. Fluid Mech.* **1005**, A14.

Watanabe, T., Jaulino, R., Taveira, R. R., da Silva, C. B., Nagata, K. & Sakai, Y. 2017*a* Role of an isolated eddy near the turbulent/non-turbulent interface layer. *Phys. Rev. Fluids* **2** (9), 094607.

Watanabe, T., Mori, T., Ishizawa, K. & Nagata, K. 2024 Scale dependence of local shearing motion in decaying turbulence generated by multiple-jet interaction. *J. Fluid Mech.* **997**, A14.

Watanabe, T. & Nagata, K. 2022 Energetics and vortex structures near small-scale shear layers in turbulence. *Phys. Fluids* **34** (9), 095114.

Watanabe, T. & Nagata, K. 2023 The response of small-scale shear layers to perturbations in turbulence. *J. Fluid Mech.* **963**, A31.

Watanabe, T. & Nagata, K. 2025 Influences of small-scale shear instability on passive-scalar mixing in a shear-free turbulent front. *J. Fluid Mech.* **1008**, A20.

Watanabe, T., Naito, T., Sakai, Y., Nagata, K. & Ito, Y. 2015 Mixing and chemical reaction at high schmidt number near turbulent/nonturbulent interface in planar liquid jet. *Phys. Fluids* **27** (3), 035114.

Watanabe, T., Riley, J. J. & Nagata, K. 2016 Effects of stable stratification on turbulent/nonturbulent interfaces in turbulent mixing layers. *Phys. Rev. Fluids* **1** (4), 044301.

Watanabe, T., da Silva, C. B. & Nagata, K. 2020*a* Scale-by-scale kinetic energy budget near the turbulent/nonturbulent interface. *Phys. Rev. Fluids* **5** (12), 124610.

Watanabe, T., da Silva, C. B., Nagata, K. & Sakai, Y. 2017*b* Geometrical aspects of turbulent/non-turbulent interfaces with and without mean shear. *Phys. Fluids* **29** (8), 085105.

Watanabe, T., Tanaka, K. & Nagata, K. 2020*b* Characteristics of shearing motions in incompressible isotropic turbulence. *Phys. Rev. Fluids* **5** (7), 072601(R).

Watanabe, T., Zhang, X. & Nagata, K. 2018 Turbulent/non-turbulent interfaces detected in DNS of incompressible turbulent boundary layers. *Phys. Fluids* **30** (3), 035102.

Watanabe, T., Zhang, X. & Nagata, K. 2019 Direct numerical simulation of incompressible turbulent boundary layers and planar jets at high Reynolds numbers initialized with implicit large eddy simulation. *Comput. Fluids* **194**, 104314.

Zhang, X., Watanabe, T. & Nagata, K. 2018 Turbulent/nonturbulent interfaces in high-resolution direct numerical simulation of temporally evolving compressible turbulent boundary layers. *Phys. Rev. Fluids* **3** (9), 094605.

Zhang, X., Watanabe, T. & Nagata, K. 2023 Reynolds number dependence of the turbulent/non-turbulent interface in temporally developing turbulent boundary layers. *J. Fluid Mech.* **964**, A8.